



A STUDY OF THE SUN IN
WHITE LIGHT

Frank E. Taylor
MIT Cambridge, MA

A STUDY OF THE SUN IN WHITE LIGHT

Frank E. Taylor

Department of Physics
Laboratory for Nuclear Science
MIT
Cambridge, Massachusetts

November 19, 2015

Abstract

Owing to its proximity a number of interesting astrophysical observations can be made by viewing the sun in the visual continuum ($420 \text{ nm} < \lambda < 700 \text{ nm}$). Among the measurements that can be made with a simple telescope, digital camera and solar filter are limb darkening, sunspot development, temperature of umbra and penumbra of sunspots, size distribution of sunspots, sidereal rotation of the sun versus solar latitude and the ellipticity of the earth's orbit around the sun. This note describes a personal study of the sun that could be a prototype for an MIT Junior Lab 8.13/8.14.

Never look directly at the sun with the unaided eye. Always use precautions to protect your eyesight and telescope equipment with proper solar filters.

Table of Contents

1 Introduction	3
2 Physics Essentials	4
2.1 Photosphere	6
2.1.1 Limb Sharpness	7
2.1.2 Limb Darkening	9
2.1.3 Sunspots	10
2.1 Top of Convection Zone	15
3 Apparatus Essentials	17
4 Analysis Chain	20
4.1 Geometry	20
4.2 Time	23
5 Results	26
5.1 Longitudinal Motion	26
5.2 Latitudinal Drift	30
5.3 Measure of Granulation	31
5.4 Discussion	31
6 Conclusions	34
7 Acknowledgements	35
8 References	36
9 Appendix A – The Data	38

1 Introduction

For a broad education in physics, study the sun. On that intellectual journey one will encounter atomic physics, thermodynamics, electricity and magnetism, gravitation, nuclear physics and the physics of neutrinos. There are few accessible measurements, other than observing the sun, where an amateur or a student can gather significant data, analyze them and observe interesting and fundamental phenomena.

By using a set of digital photographs taken with a 600 mm f/5.6 telephoto lens (Nikkor 300 mm f/2.8 lens with a Nikon 2x tele-converter with a Nikon D300s camera body [1]) or an equivalent telescope and camera through a solar light filter of optical density 5 (Thousand Oaks Optical [2]) a number of interesting observations of the sun can be made enabling a significant data set to be collected. Especially interesting is the rotation period of the sun. It is well-known that the rotation period of the solar equator is shorter than the corresponding period at higher latitudes. This differential rotation is fundamental in transforming a weak solar poloidal magnetic field into one with a strong toroidal component which in turn is responsible for the 11 year sunspot cycle. By synchronizing the camera's clock to UT for an accurate time-stamp, the motion in longitude and latitude of an ensemble of sunspots can be recorded and analyzed. By knowing the telescope's geocentric alignment the sidereal rotation of a sunspot can be determined as a function of solar latitude.

Atmospheric 'seeing' limits the resolution of pictures taken at sea level to ~ 2 to 3 arc seconds but is highly variable around Lexington MA, larger than the diffraction limit of ~ 1.4 arc seconds of the telescope used. A resolution of 2 to 3 arc seconds is adequate for observing sunspots larger than an area of roughly 15 millionth of the solar visible disk. Most prominent features of the photosphere are therefore visible at sea level under average seeing conditions but some, such as the granulation of the upper reaches of the convection layer, are at the limit of observation. Prominences, flares and coronal mass ejections and other interesting features of solar activity require observing the sun with a narrow optical filter, such as one tuned to the H- α line ($n=3$ to 2 transition at 656.281 nm).

The measurement technique and analysis of the data are given in this note. From these pictures the limb darkening can be estimated, sunspot evolution is observed, the umbral temperature of a sunspot compared to the surrounding plasma, super granules and faculae (bright regions) can be seen. And, as noted by using the UTC time stamp of the pictures and solving the spherical astronomy equations, the solar rotation rate can be determined as a function of solar latitude. In addition, the latitudinal drift rate of sunspots can be observed. The data collected in this note are compared with published analyses.

2 Physics Essentials

The sun is a gaseous sphere consisting of mostly Hydrogen (90%) and Helium (9%) with a small fraction of heavy metals (1%), heated by p-p fusion in its core resulting in a black body temperature at its photosphere of 5,777 degrees Kelvin. The density as well as the pressure of the solar gas falls exponentially with increasing radius and at the radius of the photosphere have the values of $(2-3) \times 10^{-7} \text{ gm cm}^{-3}$ and $\sim 1.1 \times 10^5 \text{ dynes cm}^{-2}$, respectively, whereas at the core of the sun has a density of 150 gm cm^{-3} and a pressure of $2.33 \times 10^{17} \text{ dynes cm}^{-2}$.

The sun has eight principal regions, described in the following table and in Fig. 1.

Table I: Standard Solar Model

Region	Inner Radius (km)	Temperature ($^{\circ}\text{K}$)	Density (gm/cm^3)	Defining Properties
Core	0	1.5×10^7	150	Energy generated by p-p fusion ($kT \sim 1 \text{ keV}$)
Radiative zone	2×10^5	7×10^6	15	Energy transported by electromagnetic radiation
Convection zone	5×10^5	2×10^6	0.15	Energy carried by convection in cells call granulation 900 to 2,000 km in diameter
Photosphere	6.960×10^5	5.8×10^3	2×10^{-7}	Thin region where photons can escape, light generated by H- recombination
Chromosphere	6.965×10^5	4.5×10^3	5×10^{-9}	Cool lower atmosphere, rose colored H emission lines, Helium (5876\AA) and ionized Calcium
Transition zone	6.98×10^5	8×10^3	2×10^{-13}	Rapid temperature increase in transition to corona
Corona	7.06×10^5	1×10^6	10^{-15}	Hot, low density upper atmosphere
Solar Wind	10^7	2×10^6	10^{-26}	Solar material (\sim protons) flowing outward through the solar system from Coronal Mass Ejections and solar flares

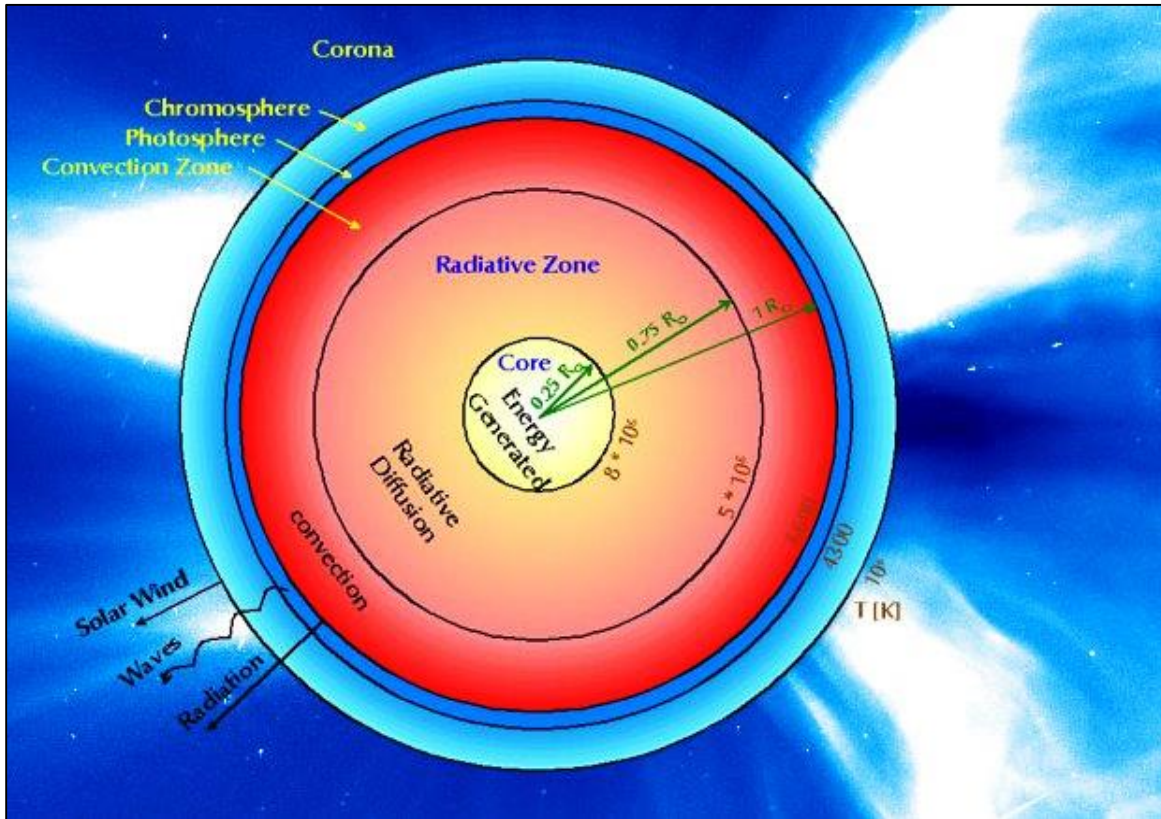


Fig. 1 shows the various regions of the sun, their temperature, radius and principal physics. The thin transition zone between the Chromosphere and Corona is not indicated. [Diagram from web.]

A number of calculations of the sun temperature, pressure, energy generation, opacity, energy output, etc. have been made leading to what is called the *standard solar model*, such as that of John N. Bahcall et al., [3]. There are many inputs to the model for which complete descriptions are beyond this note. Key is the computations of hydrostatic equilibrium, thermodynamics, nuclear physics, and atomic physics and helioseismology observations. Bahcall and collaborators have refined their well-known standard solar model over the years to the point of making a key prediction of the neutrino flux from the core of the sun. Direct observations of the neutrino flux by R. Davis [4] and collaborators, where the measured flux of solar neutrinos was stubbornly 1/3 of the predictions of Bahcall et al. [3], led to the establishment of neutrino oscillations.

In order to get a sense of the scale of densities of the sun as a function of radius the computed values in a model by Dalsgaard, et al. [5] are shown in Fig. 2. Note that the density of the photosphere is less than that of air at sea level by roughly a factor of 1/10,000, $1.22 \times 10^{-3} \text{ g/cm}^3$ vs. $2 \times 10^{-7} \text{ g/cm}^3$ for the sun. It is only deep in the radiative zone of the sun where the gas density reaches $\sim 1 \text{ g/cm}^3$.

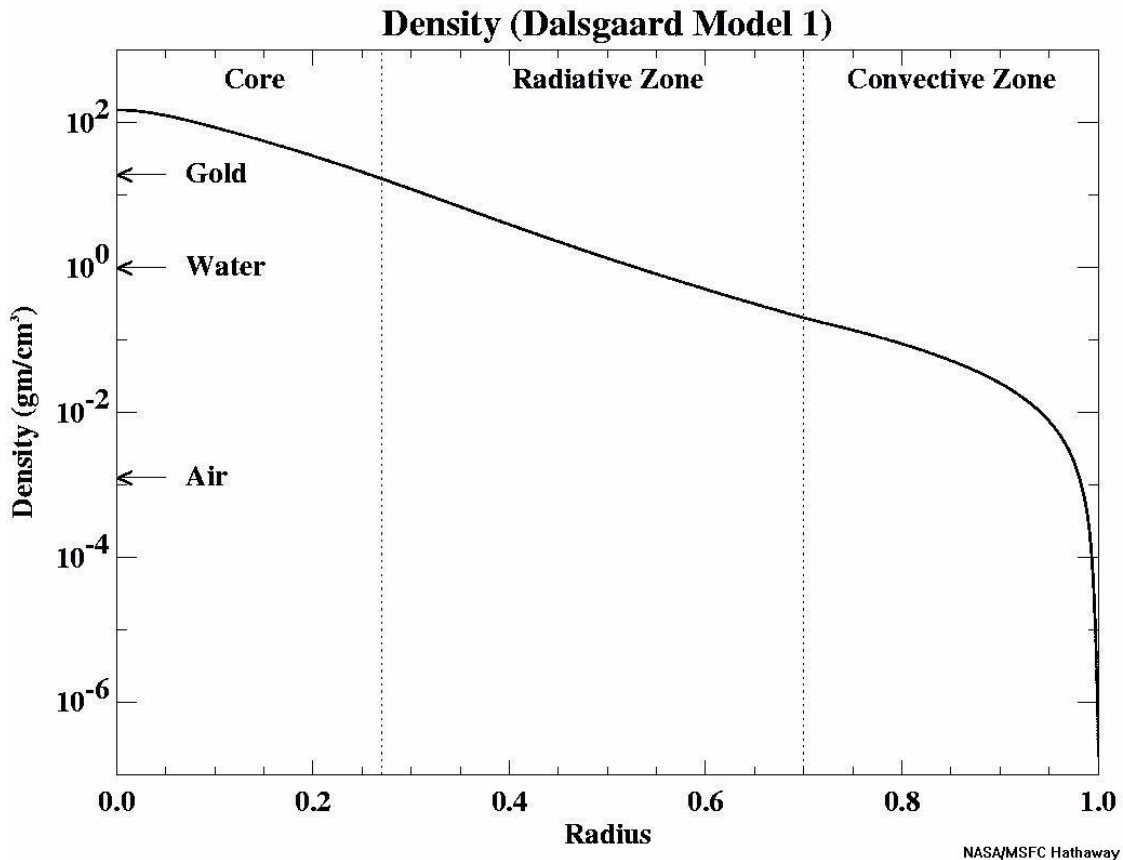


Fig. 2: The density of the sun vs. radius in the model of Dalsgaard, et al. [5] <http://solarscience.msfc.nasa.gov/interior.shtml>.

2.1 Photosphere

The solar photosphere is the region of the sun that is primarily observed in ‘white light’. Therefore it is interesting to study the physics of this region in detail. The photosphere temperature is $\sim 5,800$ K and corresponds to an average thermal energy of $3/2 kT \sim 0.75$ eV. This temperature is insufficient to significantly ionize atomic Hydrogen (13.6 eV). However, there are enough heavier metals in the gaseous mix of the sun ($\sim 1\%$) that are ionized at this photospheric average energy resulting in an excess of electrons. Since Hydrogen is so abundant H^- ions are formed with the ratio of H^-/H is $\sim 10^{-8}$. This value is seemingly a small number but it is significant because the ionization and recombination of the H^- ion are primarily responsible for the generation of the opacity of the photosphere¹.

¹ The physics of the H^- ion plays a key role in the spectrum of the photosphere. The ion absorbs photons of energy 0.75 to 4.0 eV but has only one energy level and ionizes at 0.754 eV. Its existence was proven theoretically by Bethe (1929) and a good discussion of it can be found in the classic Quantum Mechanics of One- and Two-Electron Atoms, H. A. Bethe and E. E. Salpeter, Academic Press Inc. New York (1957) [6].

2.1.1 Limb Sharpness

Photons emitted in deep and hotter layers of the sun take millions of years to find their way out of the sun through the photosphere into the darkness of space. In considering the photosphere the first question is why does the hot ball of gas with an exponentially falling density and pressure that comprises the sun have such a sharp edge in visible light? The photosphere is the outermost layer of the sun where photons are finally released.

Following Table 5.3 (Dermott J. Mullan, Physics of the Sun – A First Course, CRC Press, 2010 [7]) we find the optical depth changes radically from $2/3$ at the nominal photosphere radius to $\sim 10^{-4}$ over a height of only ~ 500 km above the photosphere, a thickness which is only ~ 0.0007 of the solar radius. Beyond the nominal photosphere radius up to about 500 km, the density and pressure of the solar gas continues to fall exponentially but the temperature stays roughly constant at $\sim 5,000$ K. Below the photosphere the absorption of photons is strong and most of the outward energy transfer is by convection because the thermal gradient is large and the opacity is large. Above the photosphere photons are not absorbed. This sharp falloff of optical depth is a consequence of the absorption and re-emission of 0.75 keV photons by the H^- ion that requires just the right temperature, density and pressure and produces the sharp optical edge.

Another way to see that the edge of the sun in visible light is quite sharp is by the following argument. Since the solar gas is in hydrostatic equilibrium both the density and the pressure scale as $\sim \exp(-h/H_p)$, where H_p has the value of $(1.2-1.4) \times 10^7$ cm (120 to 140 km). Considering two lines of sight of the sun, one right on the limb and the other at the angle where the ‘seeing’ is at the limit of 1 arc second just above the limb ($h_2 = h_1 + 730$ km) one finds the ratio of gas densities of the solar atmosphere at these two heights to be $1/270$. Since the light intensity for an optically thin layer of gas is approximated by $I \sim \tau S$, where τ is the optical depth along the line of sight and S is the local source function, the optical depth at the larger height is reduced by the same factor of $1/270$ resulting in the light intensity at the larger height to be $1/270$ of the value just at the limb. The local source function S does not change rapidly with height since the temperature in the photospheric region is roughly constant. Hence the edge of the sun is sharp.

The following table summarizes the properties of the photosphere (taken from Table 5.3 of Mullan). The canonical photosphere radius is marked in yellow where the temperature corresponds to the black body value and the optical depth $\tau = 2/3$. The temperature, pressure, density, temperature gradient, Rosseland average opacity² and height above the nominal photosphere are also tabulated.

² Taking k_λ to be the linear absorption coefficient (cm^{-1}) the opacity (cm^2/gm) is $\kappa_\lambda = k_\lambda/\rho$, where ρ is the local density. The Rosseland Mean Opacity is the opacity weighted by the derivative of the blackbody spectrum with respect to photon frequency. It gives a more useful number in describing the escape of photons from the photosphere.

Table II: Properties of the Photosphere

τ (Optical Depth)	$\exp(-\tau)$	T (K)	P (dynes/cm ²)	ρ (gm/cm ³)	dT/dz (°K/cm)	κ (cm ² gm ⁻¹)	ΔR (km)
2.00E-04	1.000	4,860	1.77E+03	5.69E-09	9.57E-08	0.0091	428.4
5.00E-04	1.000	4,860	2.47E+03	7.94E-09	1.87E-07	0.0129	392.7
1.00E-03	0.999	4,860	3.35E+03	1.08E-08	3.38E-07	0.0174	359.1
5.10E-03	0.995	4,870	7.83E+03	2.51E-08	1.52E-06	0.0331	273.5
1.01E-02	0.990	4,880	1.11E+04	3.56E-08	3.02E-06	0.0468	234.5
5.01E-02	0.951	4,950	2.67E+04	8.45E-08	1.39E-05	0.0955	146.5
1.00E-01	0.905	5,030	3.82E+04	1.19E-07	2.67E-05	0.1368	106.5
2.00E-01	0.819	5,190	5.67E+04	1.71E-07	3.95E-05	0.1479	67.5
4.00E-01	0.670	5,460	8.02E+04	2.30E-07	8.05E-05	0.2642	27.5
5.00E-01	0.607	5,590	8.89E+04	2.49E-07	9.75E-05	0.3170	14.5
6.00E-01	0.549	5,700	9.64E+04	2.64E-07	1.12E-04	0.3648	4.5
6.67E-01	0.513	5,777	9.97E+04	2.71E-07	1.20E-04	0.3942	0.0
7.00E-01	0.497	5,810	1.03E+05	2.77E-07	1.28E-04	0.4236	-4.5
8.00E-01	0.449	5,920	1.08E+05	2.87E-07	1.47E-04	0.4943	-11.5
9.00E-01	0.407	6,010	1.13E+05	2.94E-07	1.64E-04	0.5675	-17.5

Table II: τ is the optical depth (no dimensions), T is the temperature in degrees K, P is the pressure, ρ the gas density, dT/dz is the thermal gradient, κ is the Rosseland mean opacity and ΔR is the distance from the nominal photosphere surface marked by the yellow band ($\tau = 2/3$).

Note that the temperature gradient changes by a factor of 10^3 whereas the temperature itself changes by only 24%. Deeper than $\tau \sim 0.9$ energy transport is dominated by convection because of the large temperature gradient and higher opacity. See Mullan's Physics of the Sun Table 5.3 for details [7].

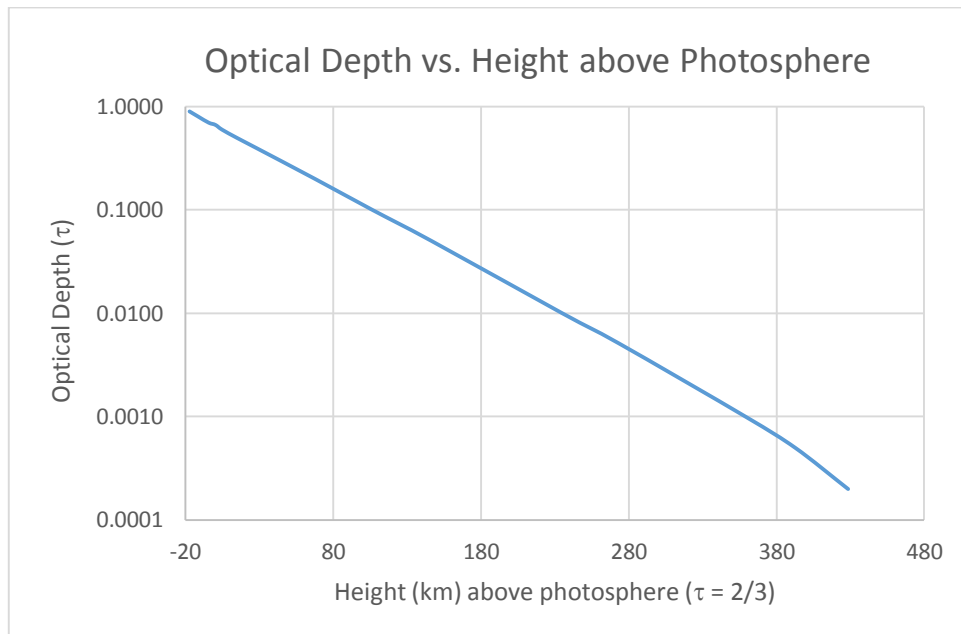


Fig. 3 The optical depth of the photosphere is shown versus the height of the nominal photosphere radius (0 on the horizontal axis) defined where the opacity is $2/3$ and the temperature is 5,777 K. Note that the photosphere thickness is less than 1,000 km, a very small fraction of the radius of the visible light sun (0.15%). The optical depth, τ , has no dimensions.

2.1.2 Limb Darkening

One of the striking features of a picture of the sun in white light is that the luminosity near the limb is smaller (darker) than at the center. Fig. 4 shows this feature along with a simple analysis of the light profile of a typical picture taken in this study.

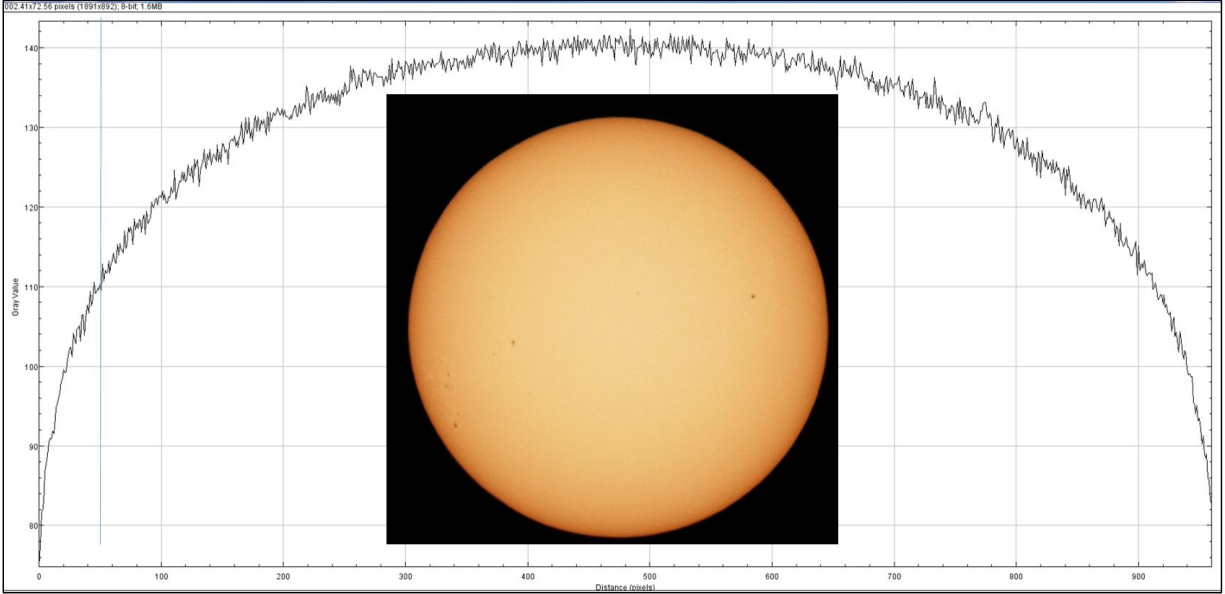


Fig. 4: A picture of the sun of this study taken 05-June-2015 in White-Light at 1/4,000 second to avoid sensor saturation through a Thousand Oaks film solar filter [2] with a Nikon D300s camera [1] set to solar white balance. The wavelength distribution of the picture is the convolution of the solar emission, atmosphere, lens and filter transmission, the camera sensitivity and picture editing bias. The limb brightness in this picture is about 57% of the center of the sun. The profile was calculated in a gray scale on the vertical axis and the distance from the left limb to the right is plotted in pixels on the horizontal axis. Several small sunspots are visible.

A full treatment of limb darkening requires solving the radiative transfer equation (RTE) of the photosphere so only a brief treatment following Mullan [7] will be given here. In the limit of small optical depth the intensity of the sun as a function of $\mu = \cos \psi$, the cosine of the angle between the line of sight and the perpendicular to the solar surface ($\mu = 1$ at center of disk and $= 0$ at limb) is given by:

$$I(t \sim 0, \mu +) = \int_0^{\infty} \frac{S(t)}{\mu} e^{-t/\mu} dt. \quad (1)$$

Eddington has analyzed the RTE for a gray solar atmosphere and found that the source function S has the form:

$$S(\tau) \sim \tau + 2/3, \quad (2)$$

and more generally (Chandrasekhar) later posited (1944) that:

$$S(\tau) \sim \tau + q(\tau), \quad (3)$$

where τ is the optical depth and $q(\tau)$ is a slowly varying function of τ ranging from 0.58 to 0.71. Note that in the blackbody approximation, the source function $S(\tau)$ can be expressed as:

$$S(\tau) = \sigma_{\text{BS}} T(\tau)^4/\pi, \quad (4)$$

where σ_{BS} is the Stefan-Boltzmann constant ($5.67 \times 10^{-5} \text{ erg cm}^{-2} \text{ s}^{-1} \text{ K}^{-4}$). The optical depth $\tau = k_{\lambda}x$, where $k_{\lambda} \sim 10^{-6} \text{ cm}^{-1}$ for $\lambda \sim 5,000 \text{ \AA}$ and x is the radiator thickness in cm. Performing the integration over t in eq. 1 one finds (like a Fourier transform):

$$I(0, \mu+) \sim 2/3 + \mu, \quad (5)$$

which predicts the ratio of brightness at the limb to that of the center of the solar disk is 0.4, in very rough agreement (0.4 vs. 0.57) with the measurement shown in Fig. 4.

Limb darkening in the visual continuum is by no means fundamental because it depends on the explicit form of the source function $S(\tau)$ which is dependent on the wavelength scale being considered. In the gray light case S increases with increasing optical depth τ given by the expression above. At other wavelengths it is possible that S decreases with increasing τ thereby resulting in limb brightening. This is observed in x-ray and extreme ultraviolet wavelengths, for example.

2.1.3 Sunspots

While the formation of sunspots has many contributing factors it is driven by the basic principle that the plasma of the sun is ‘frozen’ in the magnetic field and the poloidal magnetic field of the sun is grossly distorted by the latitudinal dependence of the solar rotation. Since the photosphere plasma of the sun has a differential equatorial rotation rate (faster at the equator than at higher latitudes) the magnetic field is dragged along and is concentrated from a weak poloidal field of a few gauss (N-S direction) to one with a strong toroidal component (E-W direction) of order several kilogauss.

The radius of the cyclotron resonance of a particle of mass m , of charge e , moving with a velocity V in a magnetic field B is:

$$r = \frac{me|V|}{|e||B|}. \quad (6)$$

Thus a charged particle will move along the B-field lines but not perpendicular to them at distance greater than the radius given above. A proton in the photosphere at temperature 6,000 K will have a velocity $|V| \sim 10^6 \text{ cm/sec}$ and thus in a $|B|$ field of 10 G the radius of gyration is $r \sim 10 \text{ cm}$. Electrons, owing to their much small mass, will have a radius much smaller.

It is interesting to note that the proton gyro-radius of 10 cm is tiny compared to any feature of the photosphere plasma, for example the scale height of the photosphere, $H_p \sim 10^7 \text{ cm}$ (100 km), noted above. It is fundamental that the magnetic field and the plasma of the photosphere move together. Although only ionized particles are affected by the magnetic field, neutral particles are

nevertheless ‘dragged’ along because they collide with the charged particles so constrained and on average are kicked in the same direction as the charged particles.

Consider an area of the plasma at constant latitude containing a given magnetic flux at the beginning of the 11 year solar cycle. Because of the Longitudinal Differential Rotation (LDR) of the photosphere, the area containing that constant flux will evolve to be more stretched in longitude and smaller in area thereby increasing the B field. See Fig. 5. Assuming that the area decreases by 10% for every rotation period at the equator (25.7 sidereal days) in roughly 5 years a starting poloidal B field of 4 G will increase to ~ 3 - 4 kG, typical for the umbra (central region) of a sunspot, and will be primarily in the E-W direction with the opposite polarity in northern vs. southern hemisphere.

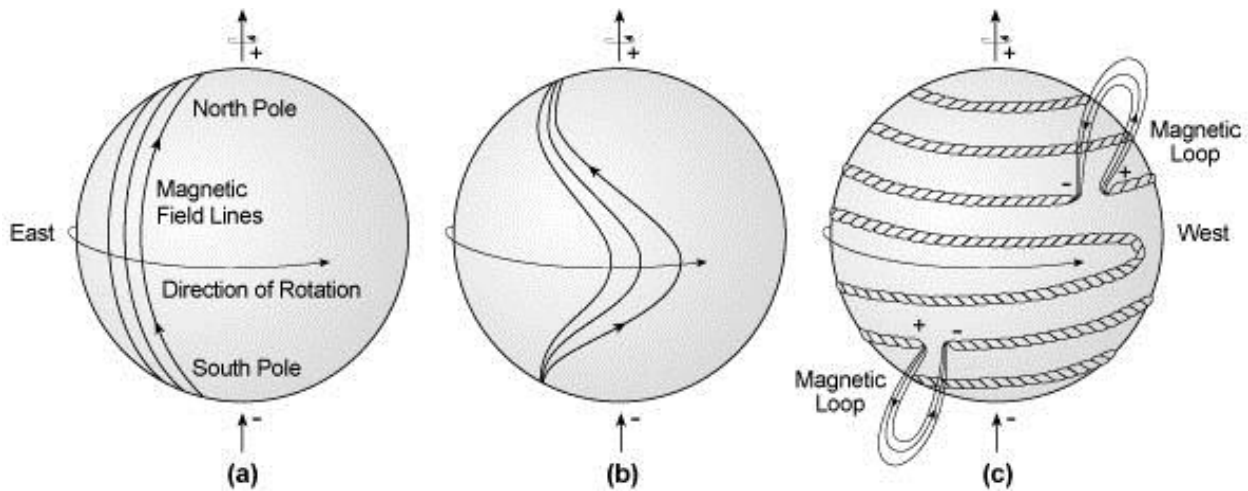


Fig. 5 Shown is the ‘winding-up’ of the solar magnetic field from a poloidal shaped field to one with a large toroidal component at three progressive times of the 11 year sunspot cycle. As is indicated in Fig. 5c, the distortion of the magnetic field makes sunspots in pairs with the magnetic polarity different in the leading and trailing sunspot as well as different in the northern vs. southern hemisphere. Note that the B-flux lines in the tubes in Fig. 5c become braided³. This leads to an increase in the magnetic stored energy. Massive solar prominences frequently show the braiding structure. [Diagram from web.]

The B-flux will concentrate in the region of maximum LDR which is computed to be between 0.9 and 0.95 of the photosphere radius initially ($6.9568 \pm 0.0003 \times 10^5$ km) and thus between 35 to 70×10^3 km below the photosphere. Since the B-flux tubes so formed constrain the plasma to move only parallel to \mathbf{B} and the magnetic pressure ($B^2/8\pi$) inside partially counteracts the surrounding gas pressure, the gas density inside a flux tube will be less than the surrounding gas. This lower gas density makes the flux tubes buoyant in the plasma and causing them to eventually bulge out in the location of the maximum field as indicated by the figure. The buoyant upward acceleration a_b is proportional to:

³ It is interesting to note that B-flux tubes can become braided and knotted. See R. L. Ricca, “Knots and Braids on the Sun”, Science and Art Sym. 2000, 263-268, A. Gyr et al. (eds.) Khwer Academic Pub. Netherlands (2000) [8].

$$a_b = g \Delta\rho/\rho \approx g B^2/(8\pi p_{\text{ext}}), \quad (7)$$

where $\Delta\rho$ is the difference of gas density outside minus inside the flux tube, ρ is the gas density outside the flux tube, g is local gravitational acceleration, B is the local magnetic field and p_{ext} is the gas pressure external to the flux tube. This bulging forms a pair of flux penetrations through the photosphere which can become a dipole of sunspots if strong enough.

The LDR is modeled to extend below the photosphere down to the bottom of the convection layer. Below the bottom of the convection zone the sun rotates as a solid body. The boundary between the part of the sun that rotates differentially with latitude and region that rotates as a solid body is called the tachocline. Fig. 6 shows the rotation as a function of depth and latitude.

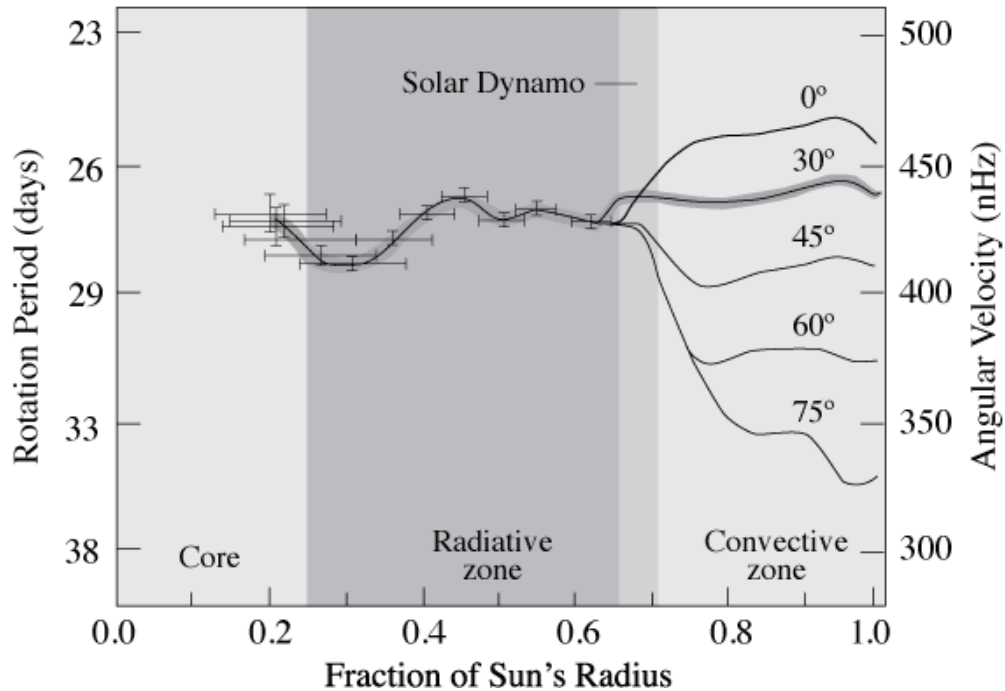


Fig. 6: The longitudinal differential rotation of the photosphere down to the bottom of the convection zone is shown. Interestingly the radiative zone and core rotate as a rigid body. Note that the fastest rotation is around the solar equator. An important input to calculating these curves is information from helioseismic data. The thin boundary between the convection zone and the radiative zone is the tachocline – that is the region of greatest shear motion and is believed to be where the sun’s B-field is generated. [Diagram from web.]

It is estimated that it takes roughly one year for the horizontal flux tubes to float through the convection zone to the surface of the photosphere and become sunspots and a few years for the stored energy in the magnetic fields to dissipate, broken apart by B-flux expulsions and reconnections and by turbulent ‘boiling’ of the convective layer. Adding the formative phase of sunspot development of 5 to 8 years, plus the buoyant phase of one year, followed by the dissipation phase the entire sunspot period is about 11 years. The magnetic polarity then reverses N-S for the next 11 years making the overall sunspot cycle 22 years.

Fig. 7 shows a high resolution picture of a sunspot taken with the Solar Dynamics Observatory (SDO) [9] which orbits the earth. (<http://sdo.gsfc.nasa.gov/data/>)

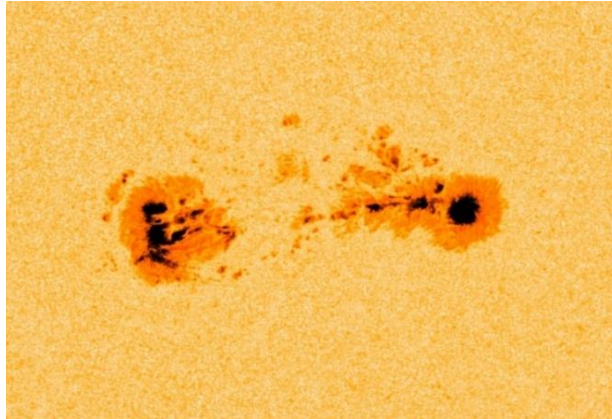


Fig. 7: A typical sunspot clump from SDO showing the umbra and penumbra as well as granulations (convective cells of the convection layer) which are typically 1,000 km in size. A telescope resolution of better than 1 arc second is needed to see the convective cells.

The temperature of the sunspot umbra is lower than the surrounding plasma because the magnetic field of the central part of a sunspot (umbra), which is primarily vertical, prevents the hotter outflowing plasma from the convection zone to immediately recirculate. As a consequence the trapped gas inside a sunspot magnetic flux tube cools more than its surroundings. A field stronger than a few kG will have so much stored energy that it can't be sustained for a long period and will eventually be released in a solar flare.

The field in the penumbra is more horizontal and less strong than the umbral value. Fig. 8a shows the B-field bulging during sunspot formation and Fig. 8b shows the B-field in the umbra and penumbra.

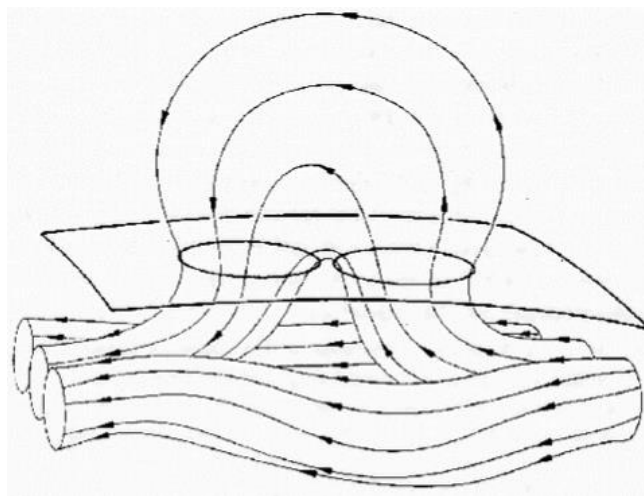


Fig. 8a shows the bulging of a flux tube that forms a sunspot pair. The height of the Ω -bulge determines the morphology of the sunspot. Flux tubes can have complicated structures by braiding and reconnections. [Diagram from web.]

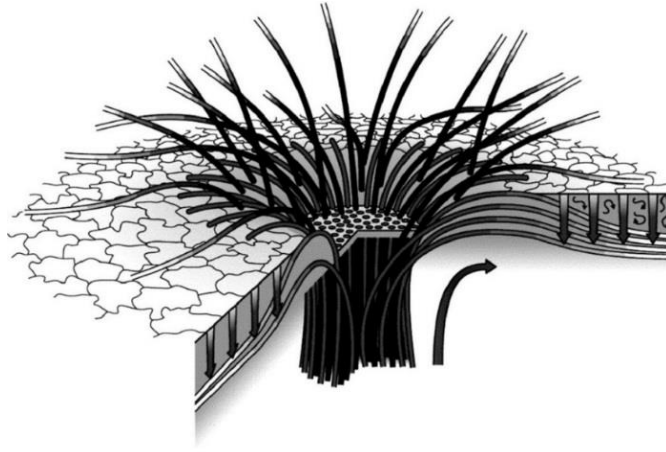


Fig. 8b shows the more vertical structure of the B-field in the umbra of a sunspot versus the more flared structure in the penumbra. Picture from Magnetic fields in the solar photosphere, Paul J. Bushby, Phil. Trans. R. Soc. A (2008) 366, 4465–4476 [10].

The temperature of a sunspot umbra can be estimated by comparing the luminosity of the umbra with that of the surrounding photosphere assuming a Stefan-Boltzmann $I(T) \sim T^4$ scaling. Fig. 9 shows a typical sunspot picture of this study (uncalibrated visible raw image) and the corresponding gray-scale luminosities of sampling rectangles. Scaling the measured intensity one estimates the temperature of the penumbra to be about 5,500 K and the umbra 4,800 K. Better calibrated bolometric measurements generally determine the temperature of the umbra to be around 4,100 to 4,200 K.

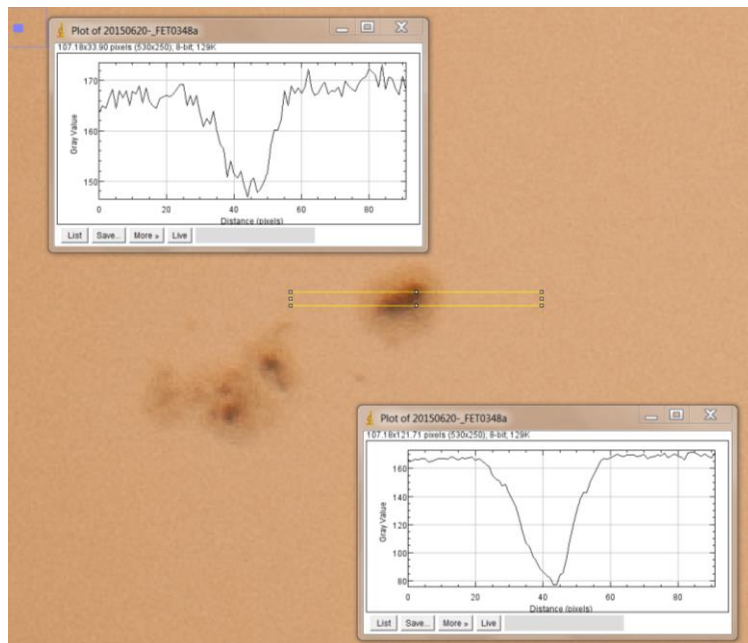


Fig. 9: The gray-scale profiles of a sunspot on 20-Jun-2015 and an expanded view of the photosphere around the sunspot group. The top profile is of the penumbra and bottom of the umbra. The total length of the sample rectangle is 90 pixels corresponding to 128,000 km. The penumbra of this sunspot is about 30,000 km in diameter. This determination finds the temperature of the umbra hotter than calibrated bolometric measurements.

At this writing (August 2015) the phase of the 11-year sunspot cycle is roughly one year beyond the peak. Fig. 10 shows the number of observed sunspots as a function of time for the present and for the last two cycles.

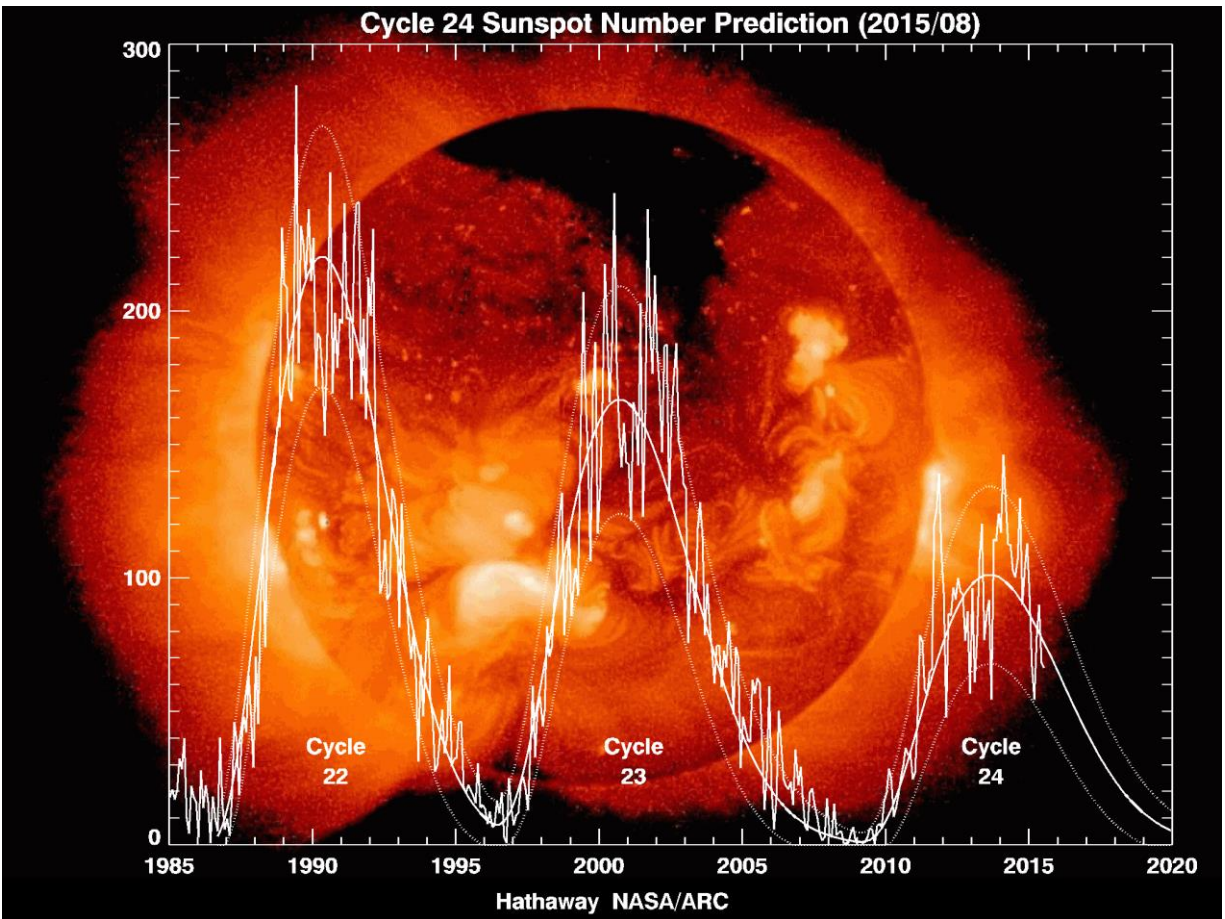


Fig. 10: We are presently in cycle 24 [11]. An algorithm exists that can predict the strength of a particular sunspot cycle. <http://solarscience.msfc.nasa.gov/predict.shtml>.

2.2 Top of Convection Zone

Since the photosphere is so thin, the top of the convection zone is visible in white light. The most obvious features are granulations, which are convective cells subtending roughly one arc-second but up to 2 to 3 arc-seconds corresponding to 1,000 to 2,000 km on the surface of the sun. This order of magnitude size is tantalizingly near the limit of the resolution of the telescope used in this study, but unfortunately only the larger granules are observable. The life-time of granules is typically 5 to 10 minutes. Fig. 7 shows the granulation around a prominent sunspot from the SDO HMI flattened images and Fig. 11 shows granulations taken with the New Solar Telescope (NST) at the Big Bear Solar Observatory (BBSO) that has an astounding resolution of 77 km on the surface of the sun [12].

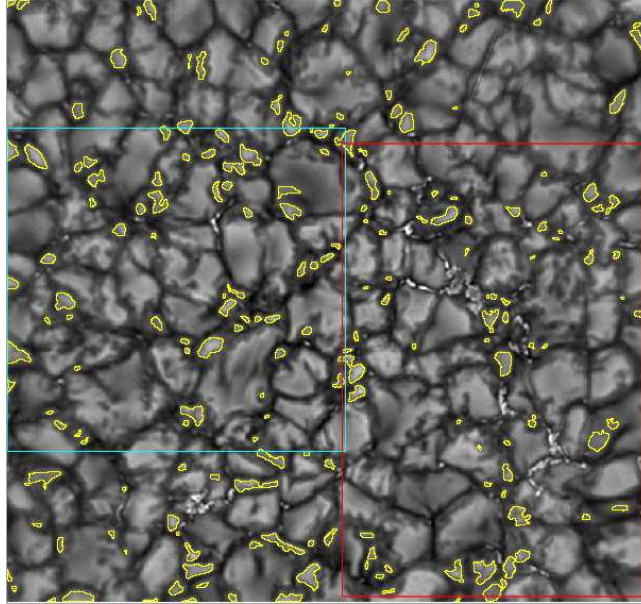


Fig. 11: An image of the convection cells of the sun taken with the NST at the BBSO. The image size is $28''.3 \times 26''.25$. See V.I. Abramenko, et al. *The Astrophysical Journal Letters*, 2012, 756, L27 [13]. The larger bright regions are locations of upwelling of hot gas and the darker regions are subsidence of cooler gas. The smaller regions outlined in yellow are identified mini-granules that have a power law size distribution.

The distribution in size of the granules is given in the same paper. Fig. 12 shows the result.

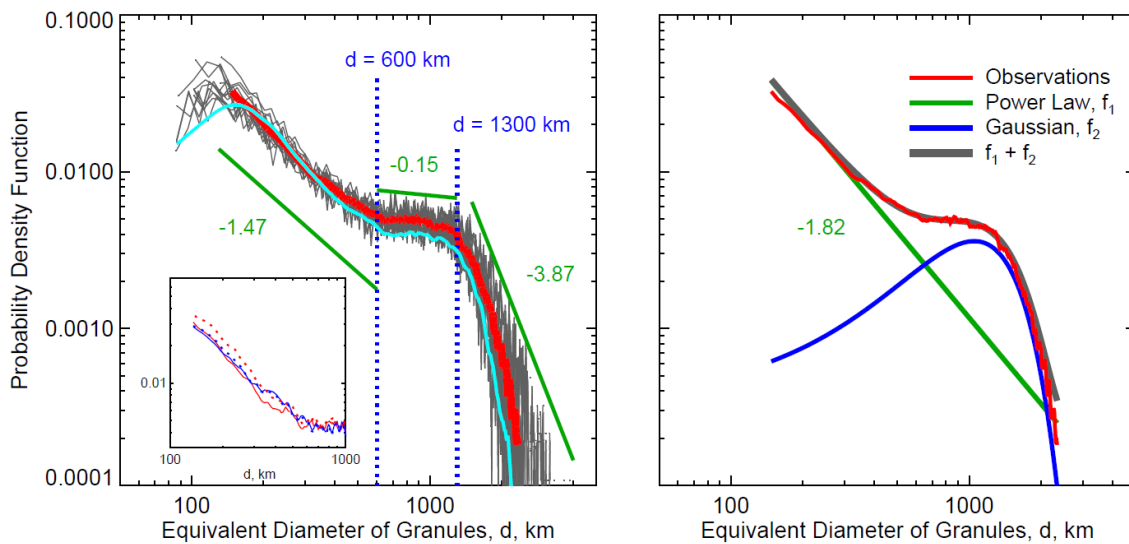


Fig. 12: The distribution of granule size as measured by the NST from ref. above. Note that there are appear to be two distribution – one a Gaussian with a mean of about 1,300 km size and another a power law $\sim 1/d^{1.82}$ with a strong falloff with increasing granule size, d.

Note there seem to be two components of the distribution of granule size – one a Gaussian with a size 1,300 km and a power law distribution of smaller granules that would be expected from a chaotic convection regime.

3 Apparatus Essentials

A Nikkor 300 mm f/2.8 lens with a 2x extender to make a 600 mm f/5.6 telescope and a Nikon D300s camera [1] were mounted on a Wimberley gimbal head – Gitzo carbon fiber tripod [14] to take daily pictures of the sun – weather permitting. The camera mount-tripod arrangement resulted in an alt-azimuth arrangement (see Fig. 13). As such it was only necessary to level the mount before each picture was taken but the time of the picture and location were needed for full analysis.

A GPS unit [15] was mounted on the camera to furnish the longitude and latitude coordinates of where the picture was taken as well as give a UTC time stamp. The GPS information was written directly into the metadata for each picture. Since most of the pictures were taken at the same location the GPS unit was not used all the time and the camera internal clock, synchronized to UTC using the US Naval Observatory time service provided the time-stamp [16]. The internal clock drifted somewhat but was kept to within < 2 seconds of UTC. For those pictures taken when the GPS was operative, the GPS UTC time stamp was used but found to generally be ~ 2 seconds late versus UTC by internet clock (a negligible error).



Fig. 13 The camera, telephoto lens, mount and solar filter covering the objective lens are shown

The alt-azimuth mount has some advantages in that it is easier to transport and does not require any astronomical alignment other than leveling (camera has an artificial horizon), but it is harder to use in that the coordinates of picture location as well as UTC must be known. As will be discussed, three angles are needed to transform the internal picture coordinates into heliocentric coordinates.

Pictures were taken in camera manual mode with a shutter speed of 1/1,600 sec, ISO 200, raw format 14 bit, f/5.6 with white balance set to “daylight”. These setting resulted in roughly 2/3 of the full exposure dynamic range of the camera. The solar light was attenuated by a Thousand Oaks Film solar filter which has an optical density of ~ 5 (attenuating the light by roughly a factor of 1/100,000). Note that the sun’s diurnal motion is 15 arc seconds/second so a shutter speed of 1/1,600th second resulted in a negligible smearing with the stationary (non-tracking) telescope.

A small amount of editing was performed on the raw image (usually 14 bit Nikon NEF format) using Adobe Lightroom® [17] to crop the picture and to enhance the contrast so that the smaller features of the picture could be more easily seen. Fig. 14 shows a typical photograph after editing. Roughly 5 to 10 pictures were taken within ~ 15 minutes and the one with the highest sharpness (smallest atmospheric turbulence) was chosen for later analysis. After editing, the pictures were saved at the highest JPEG quality allowed by the editing program.

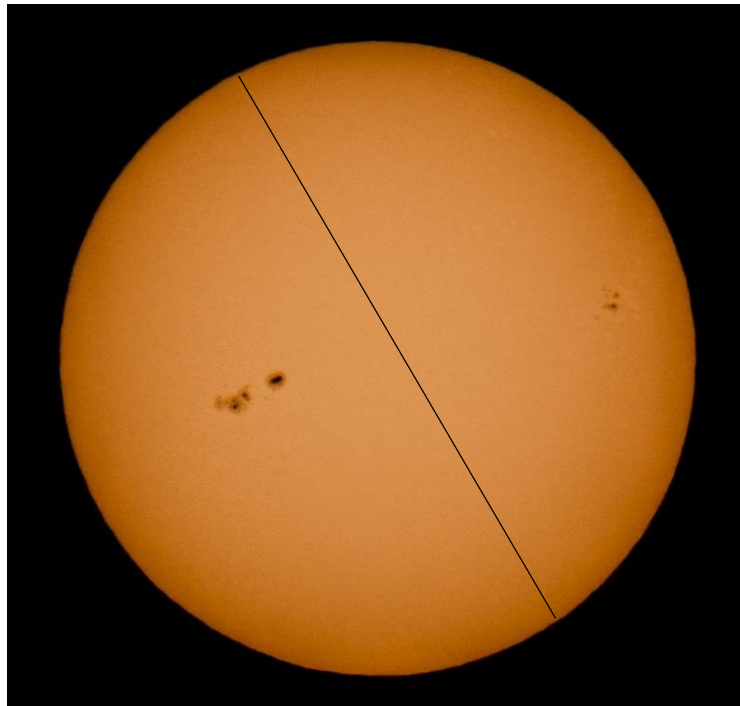


Fig. 14 A typical photograph of the sun – this taken 6/20/2015 with the alt-azimuth mounted telescope. Several large sunspots are visible with their umbra and penumbra. Limb darkening is obvious. Given the time of day at which the picture was taken, the solar rotation axis is tilted to the left at the top of the picture, the North Pole is roughly at 11 o’clock (black line) and the eastern limb is at 8 o’clock. The coordinate convention used is to call the vertical axis of the picture Z and the horizontal axis Y, pointing to the right. The X axis points toward the observer (earth). Notice the bright regions on the western limb (right side) around broken sunspots. These are faculae and are regions of hotter gas than the average photosphere.

The diffraction resolution limit of the telescope is given by [18]:

$$\varphi \sim 0.61 \frac{\lambda}{a} \sim 1.4 \text{ arc seconds}, \quad (8)$$

for $\lambda \sim 550 \text{ nm}$ and a telescope objective radius of $a = 5 \times 10^{-2} \text{ m}$.

4 Analysis Chain

The data reduction described here required many steps although the analysis could be automated (for a higher statistical study). Albeit cumbersome, this primitive method is good pedagogically in understanding all calculations.

4.1 Geometry

The first analysis step was to scan each picture using a freeware program distributed by the NIH called ImageJ [19]. Three points on the limb of the solar image were scanned to determine the image radius and center coordinates (x_0 , y_0) as well as the centroid of the umbra of the sunspot under study. The scanned information for a sunspot sequence was stored in excel files – one for each sunspot that was followed as it rotated. Some fifty sunspots were analyzed – each over several days of observations.

Once a sunspot was digitized and the information stored in its unique excel file another excel workbook was employed to compute the heliocentric coordinates for each observation day enabling a plot to be made of the longitude and latitude of the sunspot as a function of sidereal time. From these plots the rotation rate of the sun and latitudinal drift of the sunspot could be determined.

There are three angles of rotation that have to be compensated for in determining the heliocentric coordinates of the observed sunspot for the solar picture taken by an alt-azimuth mounted telescope. Two of these angles are schematically shown in Fig. 15 below – the angle P and the angle η . Both angles are relevant for the alt-azimuth and equatorial telescope mounts (see the green boxes). Referring to Fig. 15, the solar axis is indicated by the red line and the Pole-N-S line refers to earth axis. P is the position angle between the geocentric North Pole and the solar rotational North Pole measured eastward from geocentric north. The range in P is ± 26.31 degrees – the angle of the earth rotation axis with respect to the ecliptic plane. The angle η is the angle between the local zenith direction and the geocentric polar axis. Note that the parallactic angle η is largely determined by the time of day⁴.

⁴ A good description of the conventions of Heliographic coordinates can be found in W. M. Smart, Text-Book on Spherical Astronomy, Cambridge University Press, Cambridge UK (1960) [20] and the Helio v3.2 User Guide [21].

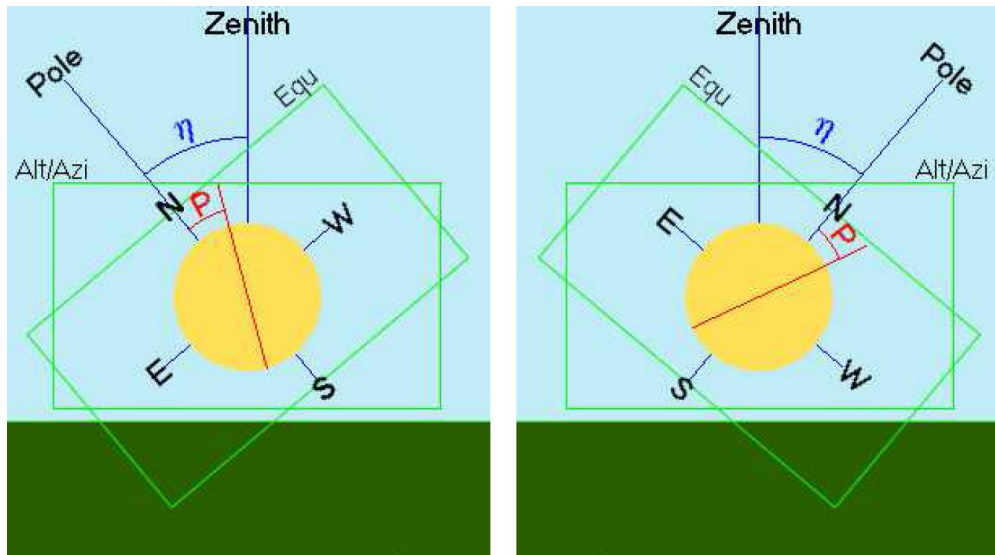


Fig. 15 The diagram is taken from Helio v3.2 User Guide [21] which is a very useful program to compute heliocentric coordinates of sunspots by Peter Meadows, September 2005. The program can be downloaded - see: <http://www.petermeadows.com/html/software.html>. The two possible telescope mountings, alt-azimuth and equatorial are shown by the green boxes. The alt-azimuth mounting scheme was used here.

The third angle B_0 is the apparent tilt of the sun's axis of rotation with respect to the ecliptic and is a function of the day of the year and ranges ± 7.25 degrees. The angle is also the Heliographic latitude of the central point (prime meridian – 0 degrees latitude) of the solar disk.

The three angles described above are sufficient to determine the latitude and apparent longitude of a sunspot. A fourth angle L_0 is used to locate the longitude of the sunspot with respect to the central point on the solar disk. Observed from the earth the central point rotates ~ 13.2 degrees per synodic day⁵.

The image rotation angles B_0 and P are tabulated in the *Astronomical Almanac* published yearly by the US Naval Observatory (<http://asa.usno.navy.mil/>) [22] and the parallactic angle η can be computed by geographic location and universal time. Much easier is to use the Helio v3.2 online algorithm <http://www.petermeadows.com/html/software.html> [21] which was done in this study although the online routine was checked several times with respect to the AA 2015. Fig. 16 shows the input/output page for the Helios routine set for an alt-azimuth telescope mount. The longitude and latitude of the telescope were inserted as is the time of the picture in UT (universal time) giving the output angles η , P and B_0 . The orientation of the picture is also displayed indicating the local zenith and the various angles.

⁵ The apparent rotation of the sun as viewed from the earth is 27.3 synodic days (period for the sun to move from prime meridian to prime meridian). In this study the angle L_0 was not computed since most of the sunspots studied were relatively short lived and generally lasted less than one solar rotation. The synodic rotation numbers 2015 are given in Table C4 of *The Astronomical Almanac for the year 2015*, Washington: U.S. Government Printing Office.

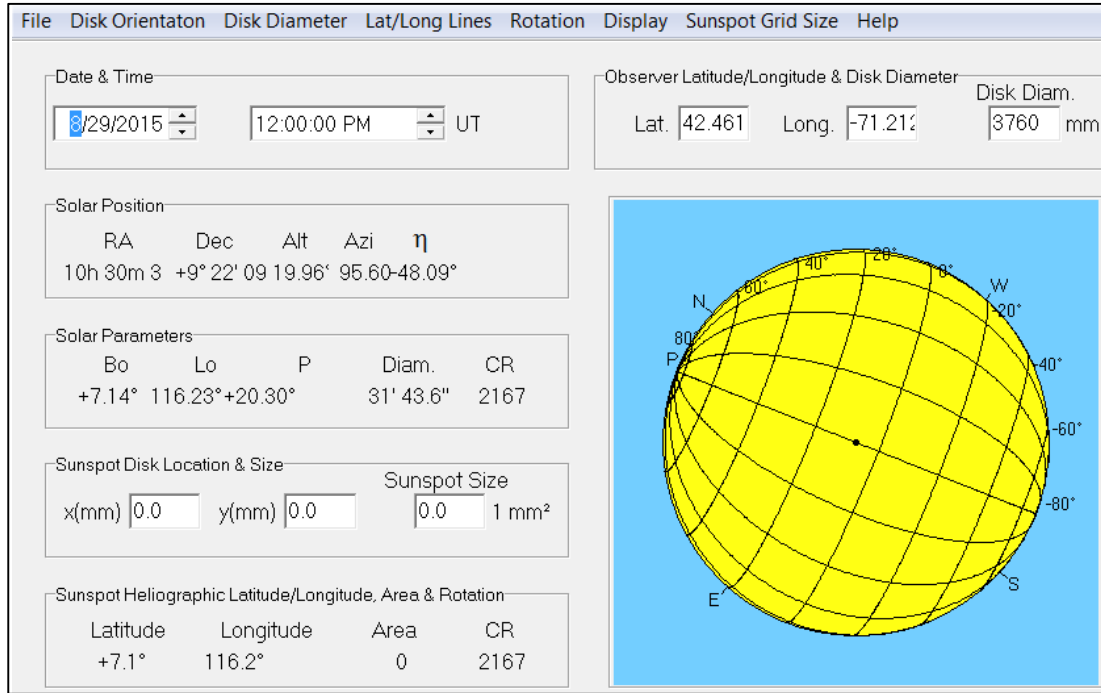


Fig. 16 The input and output of the Helios program (Peter Meadows [21]) is shown. The latitude and longitude of a putative sunspot is also displayed. The apparent diameter of the sun (Diam.) and the Carrington rotation number 1984 (CR) of the prime solar meridian are given.

The three points on the solar limb measured by ImageJ are used to calculate the radius and center coordinates of the solar image. ‘Pixel’ units of the digital photograph are used. The scanned values of the three points on the solar rim and the sunspot are then related to the center of the observed solar disk by simple coordinate translation. Next, the (x', y', z') coordinates in the image plane are determined by the following coordinate rotation:

$$z' = R_0 [z \cos(P-\eta) - y \sin(P-\eta)]/r_0 = R_0 \cos \theta' \quad (9)$$

$$y' = R_0 [y \cos(P-\eta) + z \sin(P-\eta)]/r_0 = R_0 \sin \theta' \sin \phi', \quad (10)$$

where R_0 is the known solar radius, r_0 is the measured solar radius in pixels and P and η are the angles defined above.

Solving for θ' and ϕ' given above we have:

$$x' = R_0 \sin \theta' \cos \phi', \quad (11)$$

where θ' and ϕ' and angles P and η are defined above and R_0 is the known radius of the photosphere ($6.9568 \pm 0.0003 \times 10^5$ km). Finally the rotation through the angle B_0 is performed to arrive at the heliocentric coordinates of the sunspot. This last rotation is around the y' axis and thus affects only

x' and z' coordinates to yield the coordinates of the heliocentric coordinates of the sunspot (x_s , y_s , z_s). The expressions use are:

$$y_s = y' \quad (12)$$

$$z_s = z' \cos(B_0) + x' \sin(B_0) \quad (13)$$

$$x_s = x' \cos(B_0) - z' \sin(B_0) \quad (14)$$

A number of cross checks were made – such as using the Helios program by directly entering the relative coordinate of the sunspot and by tracking the same sunspot using data obtained from the Solar Dynamics Observatory (SDO) <http://sdo.gsfc.nasa.gov/data/> satellite [9].

4.2 Time

This analysis was conducted in Sidereal time which is based on the earth's rotation rate with respect to fixed stars (not the sun). A mean sidereal day is shorter than the mean solar day and is equal to $0.99726958 = 1/(1+1/365.2422)$ mean solar days. Solar time is accurately determined by a set of atomic clocks called International Atomic Time (TAI) and is distributed by NIST and other government services. Internet time, called UTC (coordinated universal time), is measured by atomic clocks but is corrected periodically to the earth solar day and thus has an occasional leap second added because the earth rotation rate is slowly (sometimes abruptly changes by earthquake) changing. UTC differs from TAI by an integral number of inserted leap seconds (on 03-Sep-2015 TAI – UTC = 36 seconds).

See: <http://www.nist.gov/pml/div688/grp50/leapsecond.cfm>

In order to keep track of the date at which a picture of sun was taken, the Julian calendar CE is used, following the same convention as The Astronomical Almanac. Note that on January 1, 2015 the Julian date Common Era (CE) is 2,457,023.5 days and can be accessed at <http://aa.usno.navy.mil/data/docs/JulianDate.php>.

The compensation for the advance of the earth in orbit around the sun (typically $\sim 1.1135254 \times 10^{-5}$ degrees/sidereal second but varies from this average value by $\pm 3\%$ over a year by the earth's orbit ellipticity) is performed as a function Julian date. Fig. 17 shows an elliptical fit to the earth orbit for this small correction. Since a sunspot is typically observed for < 10 Julian days the average $d\theta/dt$ was used resulting in $< \pm 0.5\%$ averaging error⁶.

⁶ This correction can be refined by computing the angle advance between each successive picture rather than the overall average spanning the time between the first picture and the last of a given sunspot tracking data set.

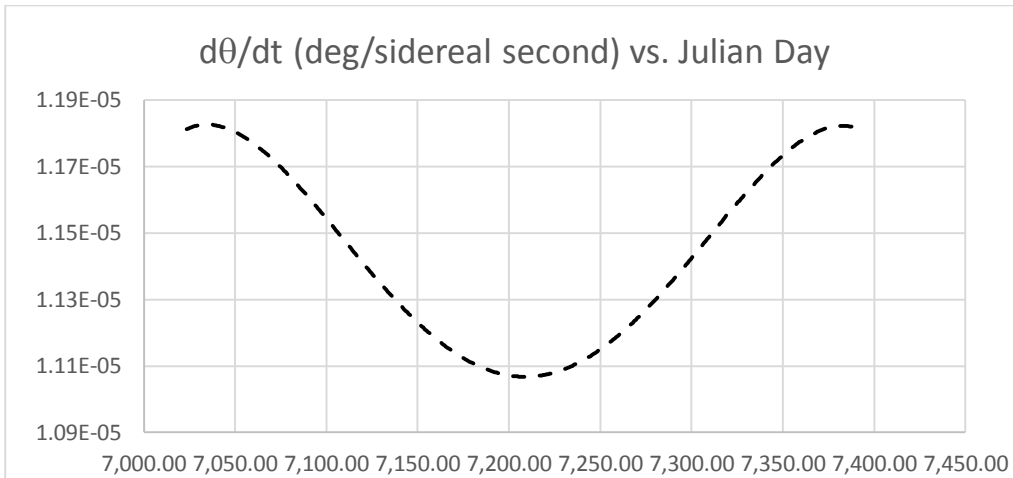


Fig. 17: The angle advance of earth degrees/sidereal second as a function of Julian date (2015).

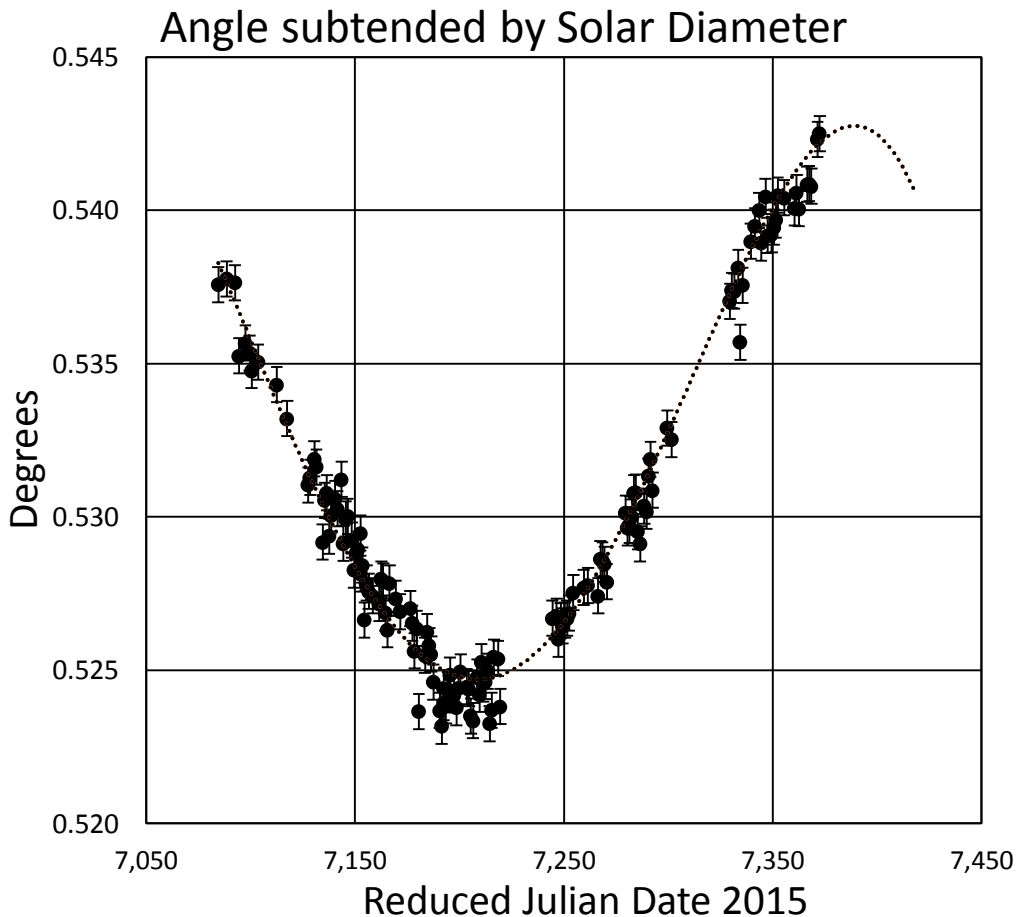


Fig. 18: The angle subtended by the solar diameter as a function of Julian date. The aphelion for these data occurred on JD 2,457,210.5. Since the telescope was not calibrated the angular scale was fixed to the known angle at aphelion. The error bars were determined from a special study of repeated measurements of the solar radius on a typical day applied to the entire data set. They are typically $\pm 0.1\%$. The earth is typically only 107 solar diameters away from the sun.

Fig. 18 shows the apparent size of the sun versus Julian date. It is interesting to note that during the course of the earth's orbiting around the sun, the apparent size of the sun varies, subtending its smallest angular size at the aphelion (for 2015 on July 7, JD 2,457,210.5 reduced to 7,210.5 on horizontal axis of figure). Tracking this variable gives an idea of the quality of the data used in this study. The sun's apparent radius is measured to $\pm 0.1\%$.

5 Results

5.1 Longitudinal Motion

Photographs were mostly taken in the early morning about 1 hour after sunrise in order to take advantage of minimum atmospheric thermal turbulence but some were taken in evening through greater turbulence when the sun's polar axis with respect to the local horizontal was completely different. Compiling the longitude as a function of sidereal time, the sidereal rotation rate is determined for a given sunspot. As a typical example, Fig. 19 shows the sunspot that was tracked. It lies in the southern hemisphere at -17.13 ± 0.44 degrees latitude.

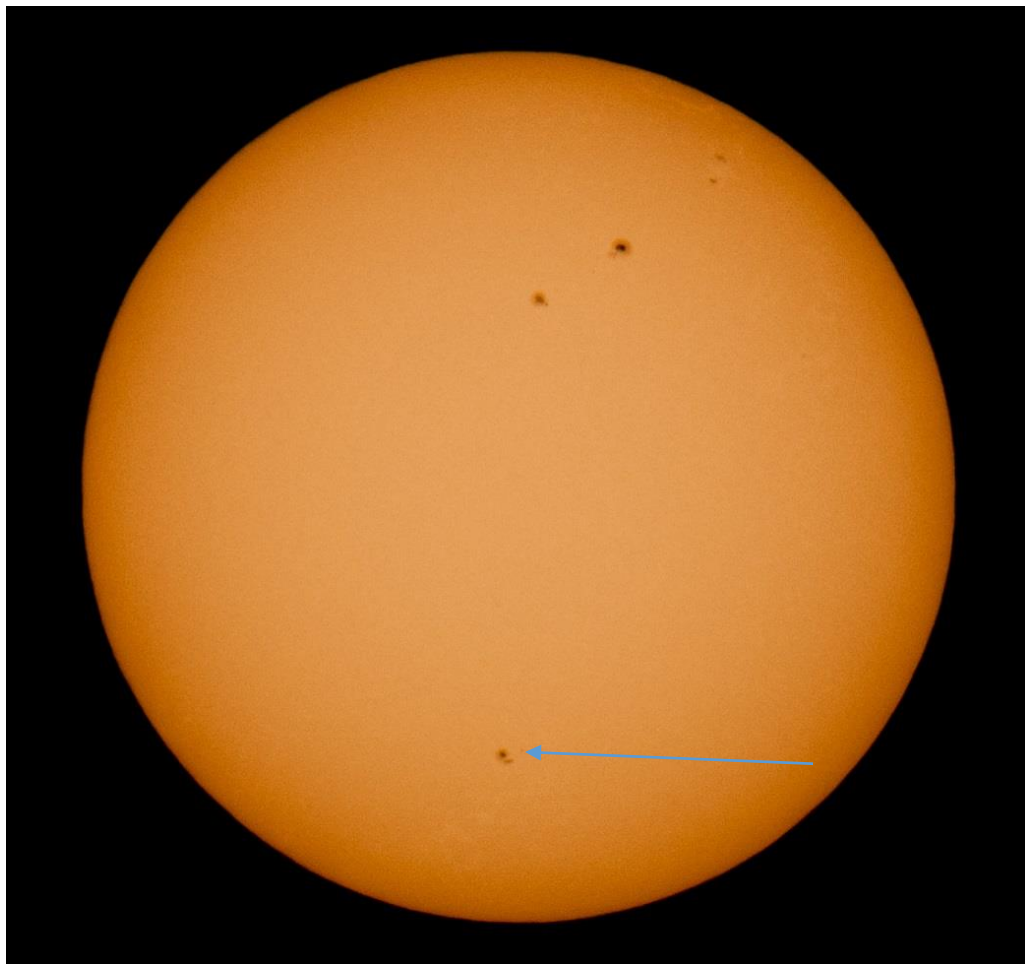


Fig. 19 is a picture of the sun taken on 12-July-2015 (Julian date CE 2,457,215.5) and the sunspot analyzed in this example is indicated by the blue arrow. This sunspot is probably 'young' owing to its intactness and small size and is typical of the sunspots analyzed in this study. The mottled regions below the bottom sunspot and around the upper most sunspot group are hotter regions, called faculae.

The longitudinal motion of this sunspot is shown in Fig. 20 below. The slope is given in degrees/sidereal second for the latitude of this particular sunspot. See figure caption for details.

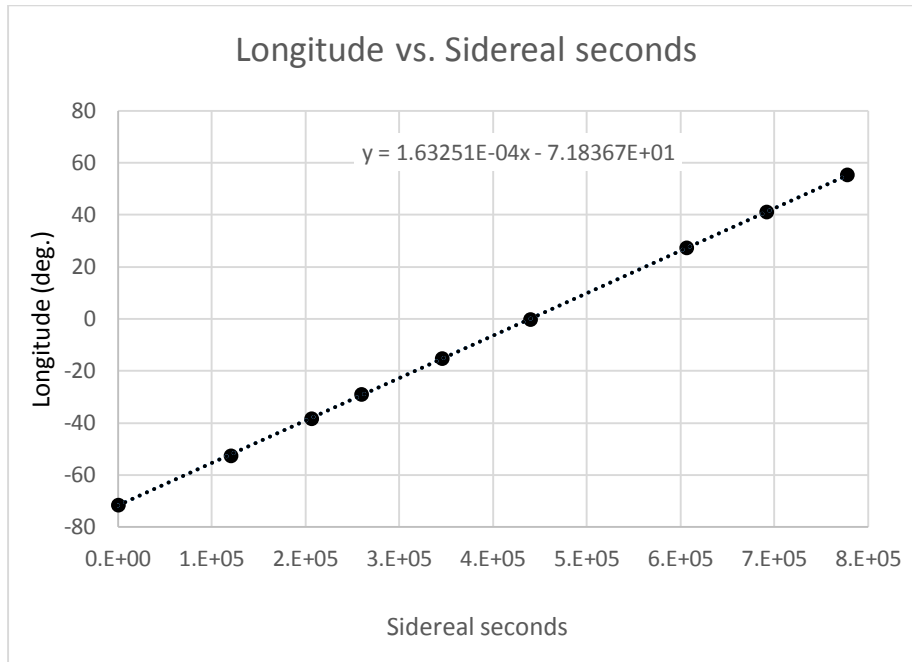


Fig. 20: The measured longitude vs. sidereal seconds of a particular sunspot is plotted. The dotted line represents a linear fit giving the rotation speed = $1.6325 \pm 0.0040 \times 10^{-4}$ deg. /sec corresponding to a rotational period of 25.52 ± 0.06 sidereal days. These data were taken July 8 through July 17, 2015. No data were taken on July 14. This sunspot <latitude> was at -17.33 ± 0.44 deg. south.

The corresponding drift of the sunspot in latitude is shown in Fig. 21.

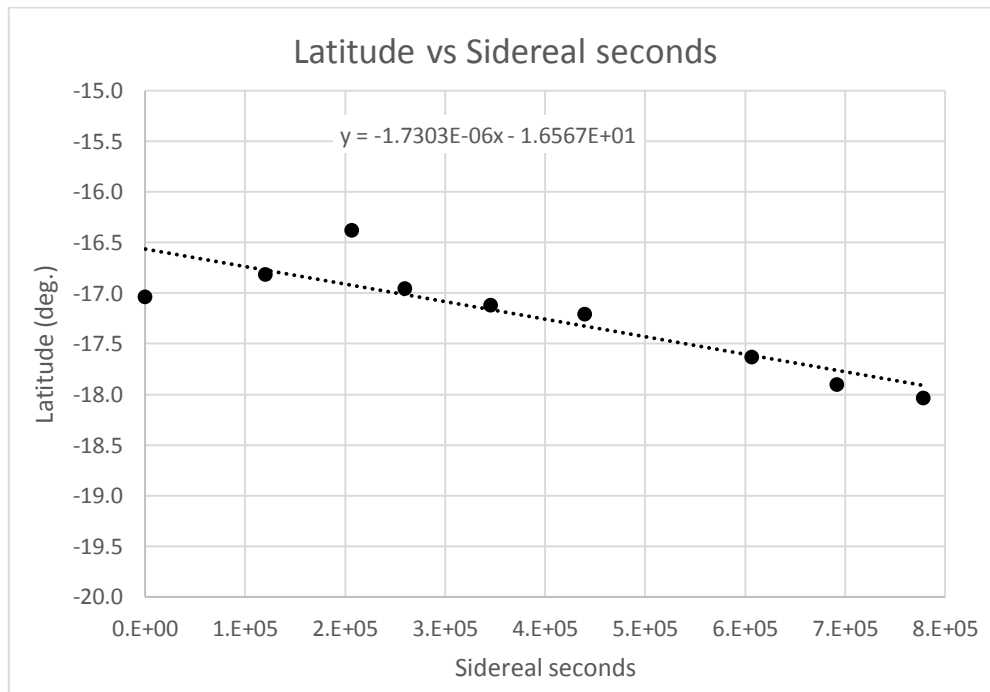


Fig. 21: The latitude of the sunspot vs. sidereal seconds is shown. For this particular sunspot there is a slow latitudinal drift = $-1.73 \pm 0.38 \times 10^{-6}$ deg. /sec.

For simplification no errors were assigned to each measurement point (although they should have been). Instead the error of the slopes vs. sidereal seconds was determined by the consistency of the points to straight lines using the MicroSoft Excel program LINEST, a least-squares routine [23].

A number of cross checks were performed in order to validate the computation of heliocentric coordinates. One validation test is obvious in looking at the data of Fig. 20, which involved separate placement and leveling of the alt-azimuth telescope for each daily observation (each data point) that resulted in a very linear dependence of the longitude vs. sidereal seconds. Another check (inadvertent) was that a sunspot was analyzed using data taken at several geographic locations which yielded consistent results with errors no larger than most of the sunspots which were observed at the same geographic (Lexington, MA) location.

Comparison analyses were made with both the telescope described here and by using images of the sun taken by SDO at nearly congruent times on 12-16 August, 2015. The comparison is given in the following table.

Table III: Comparison of this analysis with SDO

Measure	600 mm F/5.6 Telescope	Solar Dynamics Laboratory
dθ/dt (longitude) [deg/sidereal second]	$(1.673 \pm 0.013) \times 10^{-4}$	$(1.668 \pm 0.011) \times 10^{-4}$
Average Latitude [degrees]	17.47 ± 0.13	17.47 ± 0.14

Good agreement is seen in the rotation of the sun and the average latitude of the measurements. A comparison point-by-point of the latitudinal measurements are shown in Fig. 22.

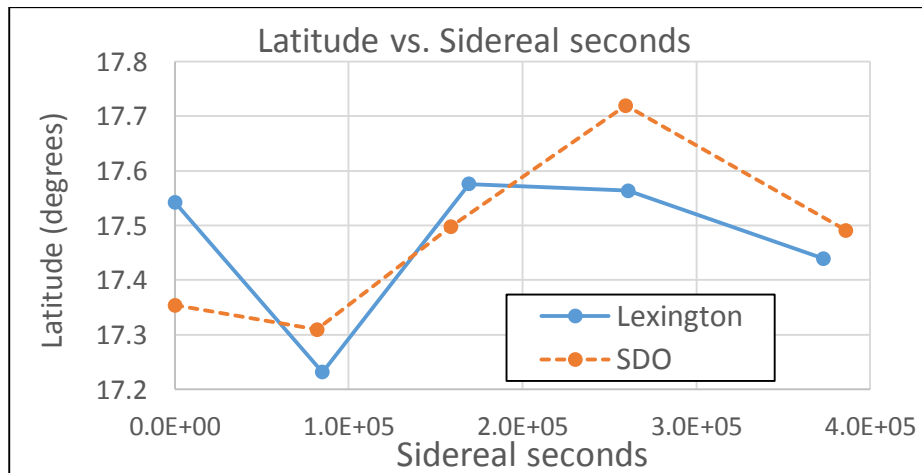


Fig. 22: A comparison of this latitude measurement (blue dots) vs. SDO (orange dotted line) for the same time interval of a typical sunspot 12-16 Aug. 2015. The two measurements track to ≤ 0.1 degree and show a larger variation than the comparison – perhaps due to the sunspot evolution and all that it entails.

The measured rotation of the sun as a function of latitude is shown in Fig. 23.

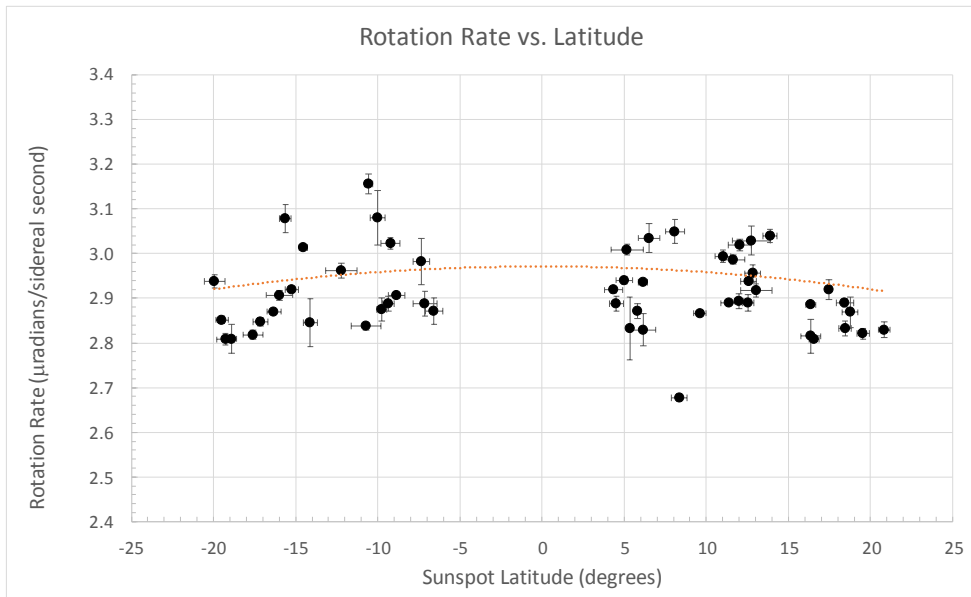


Fig. 23: The rotation rate as a function of latitude. The horizontal error for each point is the standard deviation of the distribution of latitude measurements and the vertical error bar is the error of the linear fit of the measured longitude vs. sidereal seconds. The absolute latitude data set range is 5 to 20 degrees. The colored points are 'Fit 9' (new sunspots).

And in Fig. 24 the rotation rate is plotted as function of absolute latitude.

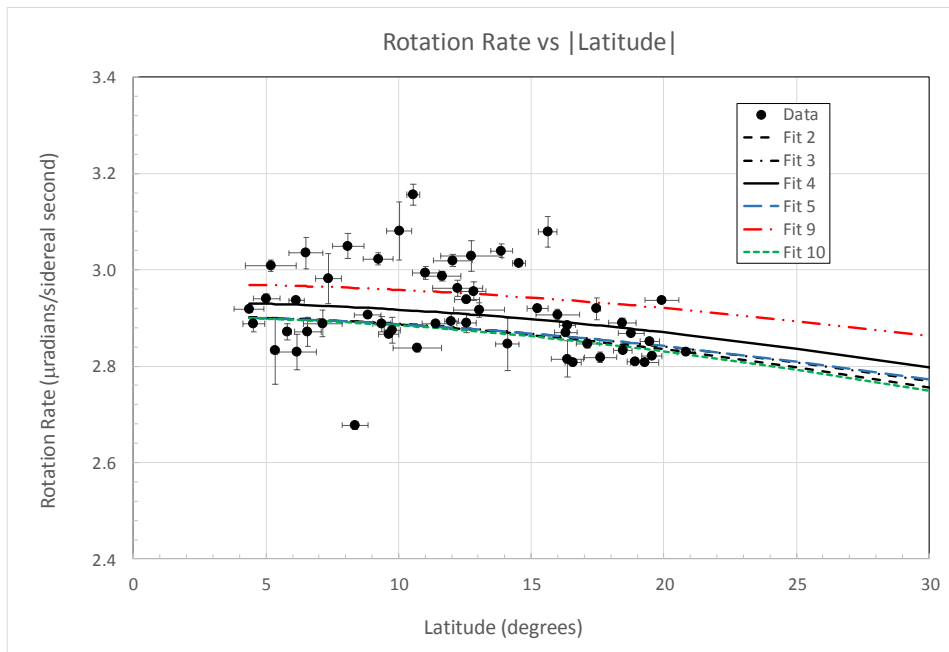


Fig. 24: Rotation rate vs. |latitude|. Several different fits as described by Beck (Solar Physics 191: 47-70, 1999) are shown. The fit to these data that most closely matches the sunspot type is 'Fit 9' based on young sunspots. Note the

large variation in the measured rotation rates – considerably beyond the estimated errors, a feature of sunspot tags determinations of the solar rotation rate.

Note that the sunspots used in this study are confined to a relatively narrow band in latitude $5 < |\phi| < 20$ degrees, whereas a more definitive determination of the latitudinal effect requires a larger latitude range. Sunspots during the earlier part of the solar cycle tend to be at higher latitudes. All these data were taken about one year (2015) past the peak of Cycle 24.

5.2 Latitudinal Drift

Figure 25 shows the measured drift in latitude for the same ensemble of sunspots. Note that the drift is quite small (a few μ degrees/sidereal second or ~ 2 degrees per rotation) but is on the edge of the experimental errors. The measured latitudinal drift seems to be limited to $< |\pm 5| \mu$ -degrees/sidereal sec. The drift in latitude is an observed feature of sunspot rotation tags but the large magnitude of the effect in these measurements was a surprise. Further study over the sunspot 11 year cycle would be interesting and may give some insight into the formation of the magnetic flux tubes that form sunspots [29].

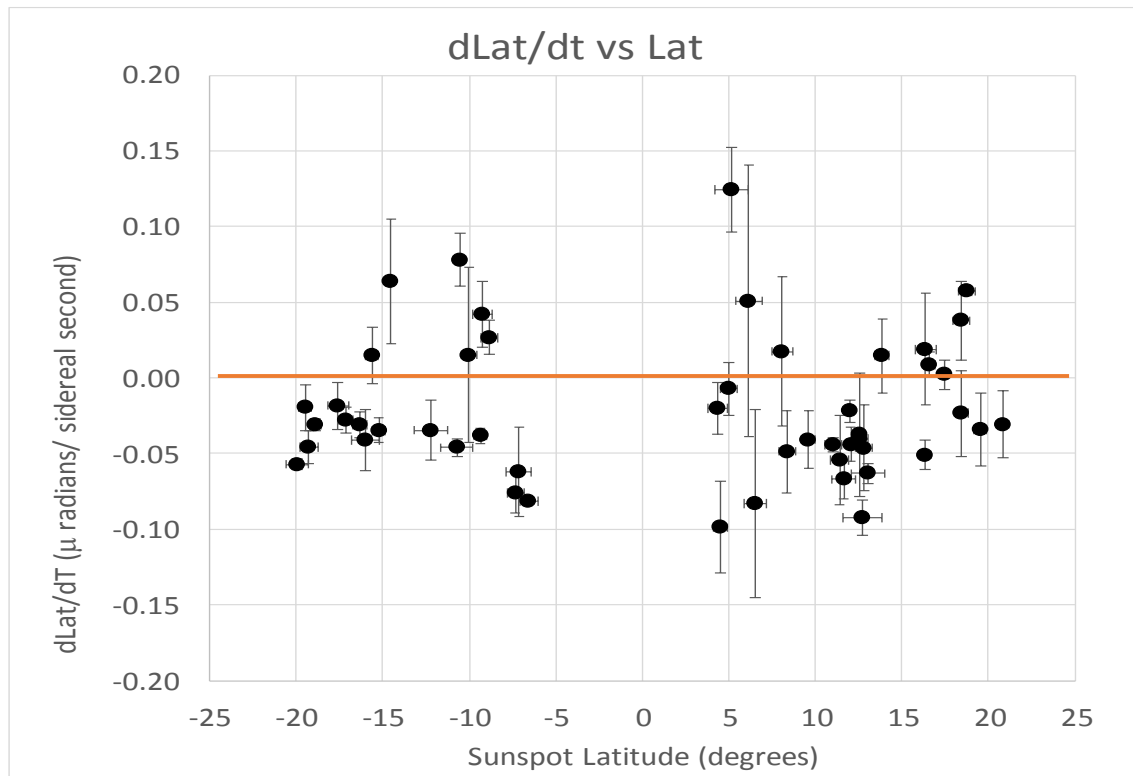


Fig. 25: The measured drift in solar latitude as a function of latitude for the same ensemble of sunspots used for the longitude motion study. The unweighted average latitudinal drift is $(1.14 \pm 1.03) \times 10^{-6}$ degrees per sidereal second – consistent with 0.

5.3 Measure of Granulation

The telescope used in this study has a pixel resolution of 1,430 km on the solar surface (1.4 arc seconds diffraction limit at 550 nm and 1.95 arc seconds/pixel). Fig. 26 shows a typical photograph of this study expanded to the pixel level. Note the brighter and less bright pixels are roughly at the right scale to be granulations.

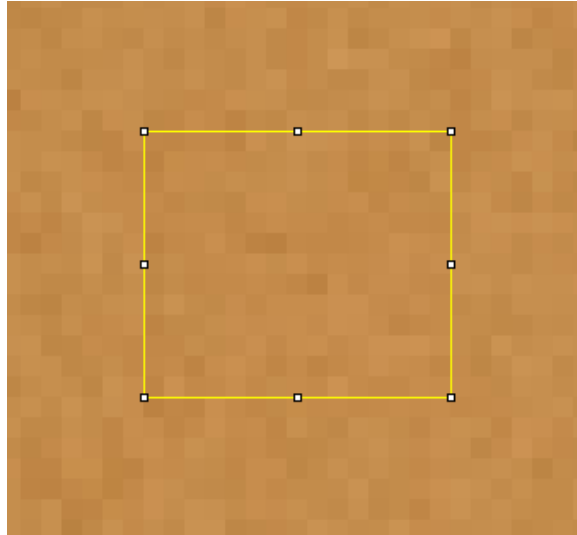


Fig. 26 shows a typical expanded view of the sun taken with the telescope of this study. The yellow box corresponds to roughly the same angular region of the NST image in Fig. 11. The picture was taken 23-Sep-15 of a region near the solar prime meridian and equator. The resolution of the limb in this picture is about 3 pixels full width or about 4,300 km on the surface of sun. Taking that number as a measure of the resolution of the picture only the largest convection cells can be distinguished.

The resolution of this study is really insufficient to see the average solar granulation. However, all pictures taken, especially at moments of ‘good seeing’ show a surface roughness - hence likely to be related to solar granulation despite the local atmospheric conditions. Plans are in the making to use a larger aperture telescope and a more fine-grained camera to sharpen this study. Furthermore, image stacking and other resolution enhancing techniques may improve the resolution sufficiently well to unambiguously observe granulation. It is interesting to note that granulations were observed by William Herschel (1801) although at the time there was much discussion about their form and function.

5.4 Discussion

The rotation of the sun has been measured for centuries – since Galileo himself observed sunspots moving across the face of the sun. There are many high statistics studies using sunspots over a long period of time (e.g. Carrington 1863 and more modern studies). A good summary is given by John G. Beck (Solar Physics 191: 47-70, 1999) [24] where spectroscopic, sunspots, super granulation tracers and helioseismology determinations are compared. What is striking about these high statistics studies, which allowed different types of sunspots to be tracked (old, new, large, small, etc.) is the wide variation ($\pm 1.7\%$) of the different rotation determinations (see Fig. 24).

The earth sidereal day, by comparison, is stable to ($\Delta T/T = \pm 2.3 \times 10^{-8}$) from 1965 to 2015 (after all it was the time standard for a few hundred years) but is influenced by tidal friction and occasional major earthquakes that are large enough to change the moment of inertia of the earth.

Using the techniques of this study a factor of 2 more data is feasible. Fig. 27a and 27b show these distributions of measured solar rotation rates and latitudinal drifts, respectively of the present 50 sunspots analyzed in this study.

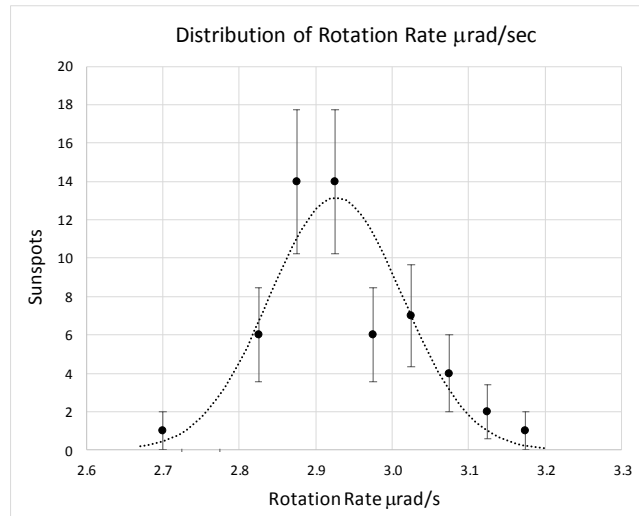


Fig. 27a: The distribution of rotation rate in $\mu\text{rad/sidereal second}$. In the overlaid Gaussian the mean $\mu = 2.914 \mu\text{rad/sidereal second}$ and standard deviation $\sigma = 0.087$.

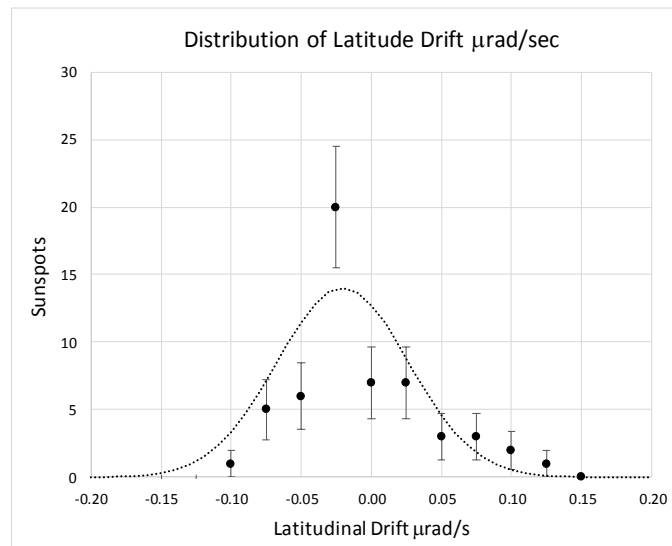


Fig. 27b: The latitudinal drift in $\mu\text{rad/sidereal second}$. In the overlaid Gaussian the mean $\mu = -0.020 \mu\text{rad/sidereal second}$ and standard deviation $\sigma = 0.047$. The average drift is consistent with 0.

One major limitation of using sunspots tracers to determine the solar rotation rate is that sunspots evolve. Small sunspots, just at the limit of observation with no penumbra, have been seen in this study to grow to become a pair of spots which develop visible penumbrae. The larger ones

sometimes split into two spots with a white bridge between the two parts, which then disintegrate into a collection of smaller spots dispersed in longitude. With a higher statistics data set certain sunspot types can be selected and de-selected but with the limited statistics of this study all ‘reasonably well-defined’ spots were used.

The measured sunspot-tag rotation rate seems to depend on the depth of the sunspot anchor – namely how deep the B-flux tube is embedded through the top of the convection layer and thereby is an indication of the plasma rotation rate at the embedded depth. Again referring to the summary by Beck, smaller sunspots tend to rotate faster than larger sunspots, lead sunspots faster than their dipole trailing sisters, younger sunspots tend to rotate faster than recurrent ones, and super granulation tends to have a different rotation signature for rotations determined by magnetic features. Doppler shifts and helioseismic period splitting yield somewhat different rotation rates (Beck [24]). While no concerted effort was made in this study to select a particular sunspot category, young and small sunspots⁷ were generally selected because they had a well-defined umbra and measurements of the sunspot rotation in this study usually commenced on East limb of the sun as the sunspot just rotated into view.

⁷ Using the ImageJ analysis program it is possible to measure the area of sunspots but this was done for only a few sunspots. The smallest area that was measured was 59 ± 16 millionths of the visible solar area and the largest was 365 ± 22 millionths of solar area. These area-data have been analyzed for only a small fraction of the sunspots used in the rotation study.

6 Conclusions

The rotation of the sun was measured using sunspot tags. Key to the formation of sunspots is the existence of the solar magnetic field frozen in the solar plasma and the differential rotation rate of the sun versus latitude – the equator rotating faster than at higher latitudes. Rotation data of 50 sunspots consisting of hundreds of photographs were collected from March 2015 until mid-September 2015.

A number of consistency checks were performed including changing the location and time of the data collection as well as comparison with the SDO satellite images. The rotation rate is consistent with the fit of Fit 9 ([25] Zappala and Zuccarello (1991 A)) for young sunspots as described in the paper by Beck within errors. In fact the average measured rotation is 2.914 ± 0.087 μ radians/sidereal second versus the average of Fit 9 of 2.948 ± 0.015 μ radians/sidereal second over the same latitude range. A fit of the rotation data of the form:

$$d\theta/dt = a + b \sin^2(\text{Lat}), \quad (15)$$

yields $a = 2.955 \pm 0.019$ and $b = -0.79 \pm 0.31$, both in μ radians/sidereal second. Hence the latitudinal dependence is measured to be non-zero to about 2.5σ . Fit 9 Beck (Zappala & Zuccarello (1991)) of young sunspots has $a = 2.972 \pm 0.002$ and $b = -0.436 \pm 0.020$ in rough agreement with this measurement. The table below summarizes this comparison.

Table IV: Comparison with Fit 9 (Zappala & Zuccarello (1991))

Units: μrad/sid sec	Lexington	Fit 9 - Z&Z
Average Rotation	2.914 ± 0.087	2.949 ± 0.015
Linear fit $a + b \sin^2(\text{Lat})$		
a	2.955 ± 0.019	2.972 ± 0.002
b	-0.79 ± 0.31	-0.436 ± 0.020

Several features of the photosphere and sunspots were observed. Limb darkening is evident in all the pictures taken in white light as is a ‘surface roughness’ attributed to the larger features of convective zone granulation. Faculae were observed near the limb in regions around sunspot activity – see Fig. 19. And a rough estimate was made of the penumbral and umbral temperature using a Stefan-Boltzmann T^4 scaling with respect to the photosphere temperature.

What was striking in this study was the large variations of the measured rotation rates and the latitudinal drifts and consequently the need for large data sets to definitively measure the average latitude dependence of the rotation rate. All these measurements are subject to their idiosyncratic dependences - for example sunspots depend on the depth of B-field flux tubes, their buoyancy, their evolving morphology and turbulence of the upper convection zone and

photosphere. A comparison of the different determinations of the rotation rate yields information about the photosphere and is of interest to the solar physicist. In fact the large variations of measured longitudinal and latitudinal drifts could be used to estimate the turbulence of the solar magnetic field on the photosphere.

It is interesting to study the origin of the solar magnetic field and source of the differential rotation of the sun above the tachocline, the thin layer separating the radiative from the convection zone – the transition between where the interior rotates as a solid body to the region where the sun has a differential rotation dependent on latitude. (See: [26] Suzanne Talon and Jean-Paul Zahn; Towards a hydrodynamical model predicting the observed solar rotation profile, *Astron. Astrophys.* 329, 315–318 (1998) and [27] Toby Wood, *The Solar Tachocline: A Self-Consistent Model of Magnetic Confinement*, Queens' College Cambridge, Ph.D. Thesis (2010).)

And it is interesting to ponder how the sun has shed its angular momentum starting with a one-day rotation period when it first entered the main sequence to a one-month period at the present time. This spin-down is dependent on the strength of the sun's magnetic field and involves magnetic field heating the corona through Alfvén waves, which in turn drives the solar wind. The solar wind is entrapped in the magnetic field and thus constitutes solar mass flung to larger radii that absorbs angular momentum. ([28] See: John H. Thomas and Nigel O. Weiss, *Sunspots and Starspots*, Cambridge University Press, Cambridge, U.K.) These aspects of solar physics, studying star-spots and a host of other plasma/astrophysics phenomena are areas of active research.

Unlike high energy physics (HEP), where theory is written in terms of fundamental Lagrangians, symmetry and conservation principles, solar physics encompasses a broad range of topics covering much of classical, nuclear, quantum physics, electrodynamics and magnetohydrodynamics - frequently on an unimaginable scale. And unlike HEP, where one studies identical particles and forces with well-defined interactions, solar physics events have their own idiosyncratic characters making their differences as interesting as their common behaviors.

7 Acknowledgements

The author thanks his colleagues for interesting discussions.

8 References

- [1] NIKON CORPORATION, Head Office Shinagawa Intercity Tower C, 2-15-3, Konan, Minato-ku, Tokyo, 108-6290, Japan; <http://www.nikon.com/about/info/corporate/index.htm>
- [2] THOUSAND OAKS OPTICAL, P.O. Box 6354, Kingman AZ 86402-6354, <http://www.thousandoaksoptical.com/solar.html>
- [3] John N. Bahcall et al., Phys. Lett. B, 433 (1998) 1-8. <http://www.sns.ias.edu/~jnb/SNdata/Export/Models/bp98stdmodel.dat>
- [4] “Measurement of the Solar Electron Neutrino Flux with the Homestake Chlorine Detector”, B. T. Cleveland, et al. The Astrophysical Journal, Volume 496, Issue 1, pp. 505-526 (1998).
- [5] “The Current State of Solar Modeling”, J. Christensen-Dalsgaard, et al, Science 31 May 1996: Vol. 272 no. 5266 pp. 1286-1292; <http://solarscience.msfc.nasa.gov/interior.shtml>
- [6] Quantum Mechanics of One- and Two-Electron Atoms, H. A. Bethe and E. E. Salpeter, Academic Press Inc. New York (1957).
- [7] Dermott J. Mullan, Physics of the Sun – A First Course, CRC Press (2010). Other good books on solar physics are:
- [7a] J. Javaraiah, M.K. Gokhole, Eds., The Sun’s Rotation, Nova Science Publications, Inc. New York (2002).
- [7b] Michael Stix, The Sun – An Introduction, Springer Berlin (2002).
- [7c] Peter V. Foukal, Solar Astrophysics, 3rd, revised edition, Wiley-VCH Verlag GmbH & Co. KGaA, Weinheim, Germany (2013).
- [8] R. L. Ricca, “Knots and Braids on the Sun”, Science and Art Sym. 2000, 263-268, A. Gyr et al. (eds.) Khwer Academic Pub. Netherlands (2000) [8]
- [9] Solar Dynamics Observatory (SDO) (<http://sdo.gsfc.nasa.gov/data/>)
- [10] Paul J. Bushby, Phil. Trans. R. Soc. A (2008) 366, 4465–4476.
- [11] An algorithm exists that can predict the strength of a particular sunspot cycle. <http://solarscience.msfc.nasa.gov/predict.shtml>. See also: David H. Hathaway, Robert M. Wilson, Edwin J. Reichmann, “The Shape of the Sunspot Cycle”, Solar Physics 151: 177-190 (1994)
- [12] Big Bear Solar Observatory (BBSO), <http://www.bbso.njit.edu/>
- [13] V.I. Abramenko, et al. The Astrophysical Journal Letters, 2012, 756, L27.
- [14] Wimberley gimbal mount (<http://www.tripodhead.com/products/wimberley-main.cfm>) on a Gitzo carbon fiber tripod (<http://www.gitzo.us/tripod>).
- [15] GeoPic II GPS unit (no longer made), http://www.bhphotovideo.com/c/product/564380-REG/Custom_Idea_GEOPICII2467_GeoPic_II_Direct_Connect.html

- [16] UTC from U.S. Naval Observatory Master Clock: <http://tycho.usno.navy.mil/simpletime.html>
- [17] Adobe Lightroom, <http://www.adobe.com/products/photoshop-lightroom.html>
- [18] Max Born, Emil Wolf; Principles of Optics, Pergamon Press (1959)
- [19] The ImageJ Program is free-ware and distributed at <http://rsb.info.nih.gov/ij/index.html>.
- [20] A good description of the conventions of Heliographic coordinates can be found in W. M. Smart, Text-Book on Spherical Astronomy, Fourth Edition, Cambridge University Press, Cambridge U.K. (1960).
- [21] Helio v3.2 User Guide, <http://www.petermeadows.com/html/location.html>.
- [22] The Astronomical Almanac for the year 2015, U.S. Government Printing Office, Washington, D.C. (2015)
- [23] MicroSoft Excel program LINEST, a least-squares routine, <https://support.office.com/en-us/article/LINEST-function-84d7d0d9-6e50-4101-977a-fa7abf772b6d>.
- [24] John G. Beck, Solar Physics 191: 47-70, (1999), and R. Casas and J. M. Vaquero, “The solar rotation in the period 1853–1870 from the sunspot catalogues of Carrington, Peters, and de la Rue”, arXiv:1410.8286v1 [astro-ph.SR] 30 Oct 2014. Table from paper with comparison of this measurement.

Table 3. The observers’ data fitted to an $\omega = a + b \cdot \sin^2(\text{Lat})$ law.

Observer	a (degrees/day)	b (degrees/day)
Carrington	14.344 ± 0.029	-2.555 ± 0.231
Peters	14.410 ± 0.024	-2.233 ± 0.220
de la Rue	14.455 ± 0.046	-2.027 ± 0.760
Lexington	14.693 ± 0.112	-4.554 ± 1.725 ← This measurement.

- [25] R. A. Zappala and F. Zuccarello, Astron. Astrophys. 242, 480-487 (1991), labeled 1991 A in Beck [24] paper.
- [26] Suzanne Talon and Jean-Paul Zahn; Towards a hydrodynamical model predicting the observed solar rotation profile, Astron. Astrophys. 329, 315–318 (1998).
- [27] Toby Wood, The Solar Tachocline: A Self-Consistent Model of Magnetic Confinement, Queens’ College Cambridge, Ph.D. Thesis (2010).
- [28] John H. Thomas and Nigel O. Weiss, Sunspots and Starspots, Cambridge University Press, Cambridge, U.K. (2008)
- [29] Jaakko Tuominen and Juhani Kyrolainen, On the Latitude Drift of Sunspot Groups and Solar Rotation, Solar Physics 79, 161-172 (1982); Jaakko Tuominen, The Latitude Drift of Sunspot Groups, Zeitschrift fur Astrophysik, Bd. 37. S 145-148 (1955).

Appendix A – The Data

Measurement Sequence	Analysis	ΔT	Size	$\sigma(\text{Size})$	λ Lat	RMS (Lat)	$d\lambda/dt$ ($\mu\text{rad/s}$)	error	Period (d)	Error Period	Lon Rate Degrees/Day	Error	nHz	Rate (rad/sec)	Lon Rate ($\mu\text{rad/sec}$)	Error
27	June SS8	4.2474E+05			-19.93	0.63	-5.71E-02	3.77E-03	24.76	0.12	14.54	0.07	467.50	2.937E-06	2.9374	0.0147
15	May AC	6.8850E+05			-19.48	0.37	-1.95E-02	1.50E-02	25.50	0.07	14.12	0.04	453.82	2.851E-06	2.8514	0.0079
48	September Lex2-1	5.2937E+05			-19.27	0.52	-4.59E-02	1.10E-02	25.90	0.12	13.90	0.06	446.85	2.808E-06	2.8077	0.0129
28	June SS9	4.2474E+05			-18.91	0.29	-3.09E-02	3.92E-03	25.89	0.29	13.91	0.16	447.05	2.809E-06	2.8089	0.0319
1	March SS1	9.4357E+05	365.40	22.45	-17.60	0.61	-1.83E-02	1.54E-02	25.80	0.10	13.95	0.05	448.53	2.818E-06	2.8182	0.0104
42	July SS11	6.9182E+05			-17.13	0.44	-2.78E-02	8.41E-03	25.54	0.08	14.09	0.04	453.10	2.847E-06	2.8469	0.0088
39	July SS8	6.3782E+05			-16.32	0.43	-3.09E-02	8.73E-03	25.34	0.05	14.21	0.03	456.80	2.870E-06	2.8702	0.0051
20	June SS1	7.6256E+05			-15.99	0.82	-4.09E-02	2.01E-02	25.02	0.09	14.39	0.05	462.64	2.907E-06	2.9069	0.0110
45	August Lex 3	6.0135E+05			-15.62	0.35	1.49E-02	1.88E-02	23.62	0.24	15.24	0.16	490.00	3.079E-06	3.0787	0.0313
49	September Lex2-2	5.2937E+05			-15.24	0.39	-3.48E-02	8.21E-03	24.91	0.06	14.45	0.03	464.68	2.920E-06	2.9197	0.0067
13	May SS1	5.7623E+05			-14.53	0.25	6.38E-02	4.12E-02	24.13	0.04	14.92	0.02	479.58	3.013E-06	3.0133	0.0046
55	November Lex2-3	1.7051E+05			-14.11	0.44	-1.10E-01	1.28E-02	25.56	0.48	14.09	0.27	452.85	2.845E-06	2.8454	0.0537
26	June SS7	6.7239E+05			-12.22	0.95	-3.45E-02	1.97E-02	24.55	0.14	14.66	0.08	471.42	2.962E-06	2.9620	0.0171
18	May AF	9.5375E+05			-10.71	0.91	-4.61E-02	5.95E-03	25.63	0.08	14.05	0.04	451.60	2.838E-06	2.8375	0.0087
35	July SS4	1.3219E+05			-10.55	0.25	7.81E-02	1.77E-02	23.05	0.16	15.62	0.11	502.22	3.156E-06	3.1556	0.0218
12	April SS6	2.1172E+11	164.89	35.78	-10.02	0.46	-1.01E-02	5.80E-02	23.61	0.46	15.25	0.30	490.24	3.080E-06	3.0803	0.0605
54	November Lex2-2	1.7051E+05			-9.76	0.30	7.59E-02	1.46E-03	25.30	0.23	14.23	0.13	457.51	2.875E-06	2.8746	0.0263
34	July SS3	6.8457E+05	186.92	32.68	-9.36	0.35	-3.83E-02	5.08E-03	25.18	0.14	14.30	0.08	459.63	2.888E-06	2.8879	0.0158
19	May AGA	4.8663E+05			-9.23	0.56	4.19E-02	2.17E-02	24.06	0.10	14.96	0.06	481.05	3.023E-06	3.0226	0.0127
11	April SS5	6.8731E+05			-8.83	0.50	2.67E-02	1.11E-02	25.02	0.05	14.39	0.03	462.50	2.906E-06	2.9060	0.0057
40	July SS9-10	2.8217E+05			-7.34	0.49	-7.60E-02	1.31E-02	24.39	0.43	14.76	0.26	474.63	2.982E-06	2.9822	0.0522
16	May AD	4.4351E+05			-7.13	0.73	-6.19E-02	2.95E-02	25.18	0.24	14.30	0.14	459.67	2.888E-06	2.8882	0.0275
41	July SS9-10	2.8217E+05			-6.57	0.51	-8.15E-02	1.77E-03	25.32	0.27	14.22	0.15	457.03	2.872E-06	2.8716	0.0301
9	April SS4	6.8840E+05			4.36	0.57	-2.02E-02	1.71E-02	24.92	0.06	14.45	0.03	464.54	2.919E-06	2.9188	0.0069
17	May AE	1.6926E+05			4.53	0.41	-9.88E-02	3.02E-02	25.18	0.14	14.30	0.08	459.62	2.888E-06	2.8879	0.0158
10	April SS4	6.8840E+05			5.01	0.51	-7.27E-03	1.73E-02	24.73	0.08	14.56	0.05	467.99	2.940E-06	2.9405	0.0091
47	September Lex1-2	3.4936E+05			5.18	0.97	1.24E-01	2.83E-02	24.17	0.09	14.89	0.06	478.87	3.009E-06	3.0088	0.0116
53	November Lex 2-1	1.7051E+05			5.34	0.14	-3.44E-02	5.45E-03	25.68	0.63	14.02	0.35	450.77	2.832E-06	2.8322	0.0699
51	November Lex1-1	4.2294E+05			5.81	0.14	-1.41E-03	8.66E-03	25.33	0.14	14.21	0.08	456.96	2.871E-06	2.8712	0.0163
52	November Lex1-2	4.2294E+05			6.14	0.28	-2.95E-02	6.32E-03	24.77	0.05	14.54	0.03	467.30	2.936E-06	2.9362	0.0057
25	June SS6	2.5874E+05			6.16	0.74	5.09E-02	8.94E-02	25.70	0.33	14.01	0.18	450.30	2.829E-06	2.8293	0.0361
46	September Lex1-1	3.4936E+05			6.51	0.64	-8.31E-02	6.18E-02	23.96	0.26	15.02	0.16	482.99	3.035E-06	3.0347	0.0331
24	June SS5	3.3232E+05			8.09	0.59	1.74E-02	4.94E-02	23.85	0.21	15.10	0.13	485.33	3.049E-06	3.0494	0.0264
5	April SS2	3.4184E+05	220.29	26.01	8.35	0.48	-4.86E-02	2.71E-02	27.16	0.08	13.25	0.04	426.15	2.678E-06	2.6776	0.0082
4	April SS2	3.4184E+05	92.89	18.52	9.62	0.38	-4.08E-02	1.89E-02	25.37	0.06	14.19	0.03	456.18	2.866E-06	2.8663	0.0063
29	June SS10	6.8941E+05			11.02	0.49	-4.40E-02	4.76E-03	24.29	0.11	14.82	0.07	476.47	2.994E-06	2.9937	0.0137
43	July SS12	3.4641E+05			11.41	0.53	-5.44E-02	2.95E-02	25.17	0.03	14.30	0.02	459.77	2.889E-06	2.8888	0.0031
14	May AB	5.1948E+05			11.65	0.69	-6.70E-02	1.28E-02	24.35	0.09	14.79	0.05	475.36	2.987E-06	2.9868	0.0106
50	September Lex 3	4.4383E+05			11.99	0.25	-2.19E-02	7.64E-03	25.13	0.15	14.32	0.08	460.52	2.894E-06	2.8935	0.0171
36	July SS5	6.8457E+05			12.04	0.72	-4.39E-02	1.15E-02	24.08	0.10	14.95	0.06	480.55	3.019E-06	3.0194	0.0126
33	July SS2	2.5317E+05			12.56	0.36	-3.75E-02	4.10E-02	25.17	0.17	14.31	0.10	459.91	2.890E-06	2.8897	0.0193
31	June SS10	6.8941E+05			12.57	0.48	-4.01E-02	4.33E-03	24.76	0.04	14.54	0.02	467.51	2.937E-06	2.9374	0.0050
37	July SS6-7	6.9618E+05			12.74	1.14	-9.24E-02	1.16E-02	24.01	0.26	14.99	0.16	482.08	3.029E-06	3.0290	0.0323
3	April SS1	3.4184E+05	58.63	15.94	12.83	0.48	-4.61E-02	2.87E-02	24.60	0.16	14.63	0.09	470.41	2.956E-06	2.9557	0.0190
30	June SS10	6.8941E+05			13.03	0.96	-6.31E-02	6.80E-03	24.93	0.13	14.44	0.07	464.29	2.917E-06	2.9172	0.0150
21	June SS2	4.0209E+05			13.88	0.41	1.47E-02	2.46E-02	23.93	0.12	15.05	0.07	483.73	3.039E-06	3.0394	0.0148
32	July SS1	2.5317E+05			16.35	0.30	-5.08E-02	9.68E-03	25.21	0.04	14.28	0.02	459.18	2.885E-06	2.8851	0.0049
23	June SS4	4.0209E+05			16.37	0.61	1.88E-02	3.70E-02	25.83	0.34	13.93	0.18	448.00	2.815E-06	2.8149	0.0372
38	July SS6-7	6.9618E+05			16.58	0.31	8.80E-03	8.23E-03	25.90	0.04	13.90	0.02	446.89	2.808E-06	2.8079	0.0043
44	August Lex 2	3.7292E+05			17.47	0.13	2.09E-03	9.87E-03	24.91	0.19	14.45	0.11	464.60	2.919E-06	2.9192	0.0228
22	June SS3	4.0209E+05			18.44	0.51	3.79E-02	2.58E-02	25.16	0.08	14.31	0.05	459.96	2.890E-06	2.8900	0.0094
6	April SS3	3.4184E+05			18.45	0.36	-2.34E-02	2.84E-02	25.68	0.15	14.02	0.08	450.75	2.832E-06	2.8321	0.0166
2	March SS2	3.4412E+05	216.74	27.98	18.77	0.48	5.74E-02	3.02E-03	25.35	0.31	14.20	0.17	456.57	2.869E-06	2.8687	0.0345
7	April SS3	3.4184E+05			19.55	0.38	-3.42E-02	2.42E-02	25.78	0.11	13.97	0.06	448.98	2.821E-06	2.8210	0.0118
8	April SS3	3.4184E+05			20.84	0.34	-3.08E-02	0.00E+00	25.70	0.16	14.01	0.09	450.32	2.829E-06	2.8294	0.0176